Liquid Metals Heat-Pipe solution for hypersonic air-intake leading edge: Conceptual design, numerical analysis and verification

Acta Astronautica 197 (2022) 336–352

Contents lists available at ScienceDirect

Acta Astronautica

journal homepage: www.elsevier.com/locate/actaastro

Liquid Metals Heat-Pipe solution for hypersonic air-intake leading edge: Conceptual design, numerical analysis and verification

Roberta Fusaro [a,*], Davide Ferretto [a], Nicole Viola [a], Roberto Scigliano [b], Valeria De Simone [b], Marco Marini [b]

[a] Politecnico di Torino (PoliTO), Turin, Italy
[b] Italian Aerospace Research Centre (CIRA), Capua, Italy

ARTICLE INFO

Keywords:
Hypersonic civil transport
Thermal protection system
Liquid metal heat pipe

ABSTRACT

Embedded propulsion systems will allow future hypersonic aircraft to reach amazing levels of performance. However, their peculiar small-radius air-intake leading edges pose serious challenges from the aero-thermodynamic, design, integration, and manufacturing standpoints. This paper discloses the methodology developed in the framework of the H2020 STRATOFLY project and specifically tailored to support the conceptual and preliminary design phases of future high-speed transportation systems. The methodology implements an incremental approach which includes multi-fidelity design, modelling and simulation techniques. The specific application to the MR3, a Mach 8 waverider configuration with an embedded dorsal mounted propulsive sub-system, is reported. Different alternative solutions have been thoroughly analysed, including five liquid metals as fluids (Mercury, Caesium, Potassium, Sodium and Lithium) and relative wick and case materials (Steel, Titanium, Nickel, Inconel® and Tungsten) and three leading-edges materials (CMC, Tungsten with low emissivity painting and Tungsten with high emissivity painting). The analysis of the heat transfer limits (the capillary, entrainment, viscosity, chocking and boiling limits) carried out for all five fluids and relative compatible materials, together with a more accurate FEM analysis, suggest the adoption of a Nickel–Potassium liquid metal heat pipe completely integrated in a platelet air-intake leading edge made of CMC material. Ultimately, the effectiveness of the adopted solution throughout all mission phases has been verified with a detailed numerical model, built upon an electrical analogy.

1. Introduction

The worldwide incentive to reconsider commercial hypersonic transport urges Europe to assess the potential of civil high-speed aviation with respect to technical, environmental, and economic viability in combination with human factors, social acceptance, implementation, and operational aspects. In this context, one of the main technical challenges is certainly represented by the high thermal loads experienced by the aircraft throughout the mission. Investigations carried out in a series of EC-funded research projects have permitted maturing a number of feasible hypersonic aircraft configurations, reaching high-level of aero-thermal-propulsive integration: LAPCAT I/II [1], ATLLAS I/II [2], HIKARI, HEXAFLY [3], HEXAFLY-International [4–7]. In 2018, the European Commission confirmed the financial support to continue these investigations in the context of the H2020 STRATOFLY Project (Stratospheric Flying Opportunities for High-Speed Propulsion Concepts). Benefitting from the heritage of the previous European projects and selecting the LAPCAT MR2.4 (Mach 8, waverider configuration) vehicle and mission as reference, the H2020 STRATOFLY project aims at further investigating the concept, through dedicated multi-disciplinary design methodologies, highly integrated subsystems design, high-fidelity simulations, and test campaigns [8]. In addition, socio-economic and environmentally sustainable aspects are specifically investigated [9].

Among the various technical challenges dealt with in the framework of the H2020 STRATOFLY Project, the thermal aspects [10] and specifically the thermal protection of leading-edge surfaces represents a crucial issue, potentially threatening the overall technical feasibility of the concept. As already anticipated, in previous international aerospace research activities, including the well-known National AeroSpace Programme (NASP), a very effective solution for leading edge protection can consist in coupling high-temperature materials with specially tailored, highly integrated heat-pipes [11–17]. According to Ref. [18], a

* Corresponding author.
E-mail address: roberta.fusaro@polito.it (R. Fusaro).

https://doi.org/10.1016/j.actaastro.2022.05.034
Received 18 October 2021; Received in revised form 26 February 2022; Accepted 23 May 2022
Available online 27 May 2022

Greek symbols

$\Delta P_{\perp}$	perpendicular hydrostatic pressure drop in $[N/m^2]$
ΔP_c	capillarity pressure differential between vapor and liquid phases $[N/m^2]$
$\Delta P_{\parallel}$	axial hydrostatic pressure drop $[N/m^2]$
ΔT	overall temperature difference between the heat source and the heat sink [K]
ε	wick conductivity factor [−]
E	emissivity [−]
θ	wicking angle [rad]
λ	latent heat of vaporization of the working fluid [J/kg]
μ_l	dynamic viscosity of the liquid phase of the working fluid [Pa s]
μ_v	dynamic viscosity of the vapor phase of the working fluid [Pa s]
ρ_{cont}	density of the heat pipe container $[kg/m^3]$
ρ_l	density of the liquid phase of the working fluid $[kg/m^3]$
ρ_v	density of the vapor phase of the working fluid $[kg/m^3]$
ρ_w	density of the wick $[kg/m^3]$
σ	surface tension of the fluid [N/m]
ψ	pipe installation angle [rad]

Latin Symbols

A_{hp}	cross-section area of the overall heat pipe $[m^2]$
A_e	area of the evaporator section $[m^2]$
A_w	wick cross-section $[m^2]$
c	sound speed of the working fluid $[m/s]$
$c_{P\,cont}$	container material specific heat at constant pressure [J/kg K]
c_{Pw}	wick material specific heat at constant pressure [J/kg K]
F_l	equivalent friction coefficient for the liquid phase of the working fluid $[m^4/s]$
F_v	equivalent friction coefficient for the vapor phase of the working fluid $[m^4/s]$
f_{Re}	reference friction coefficient $[m^{-1}]$
g	gravity acceleration $[m/s^2]$
H_l	wicking factor $[m^2]$
K	wick permeability $[m^2]$
K_{eff}	overall heat pipe effective conductivity [W/m K]
k_{cont}	thermal conductivity of the heat pipe container [W/m K]
k_{eff}	effective liquid/wick conductivity [W/m K]
k_l	thermal conductivity of the liquid phase of the working fluid [W/m K]
k_w	thermal conductivity of the wick [W/m K]
L_a	length of the adiabatic section of the heat pipe [m]
L_c	length of the condenser section of the heat pipe [m]
L_e	length of the evaporator section of the heat pipe [m]
L_{eff}	effective heat pipe length [m]
l_{hp}	real heat pipe length [m]
$l_{support}$	length of the heat pipe structural support [m]
M_v	Mach number of the flow of the vapor phase of the working fluid [−]
n	load factor [−]
$p_{evaporator}$	pressure of the working fluid in the evaporator section [Pa]
$p_{fluid_{critical}}$	pressure of the working fluid at its critical point [Pa]
Q	overall heat transfer rate [W]
$q_{capillarity}$	heat transport capillarity limit [Wm]
q_{Max}	maximum heat flux managed by the heat pipe $[W/m^2]$
$q_{Max_{boiling}}$	maximum heat flux that the heat pipe can reject considering boiling limitations $[W/m^2]$
$q_{Max_{capillarity}}$	maximum heat flux that the heat pipe can reject considering capillarity limitations $[W/m^2]$
$q_{Max_{chocking}}$	maximum heat flux that the heat pipe can reject considering chocking limitations $[W/m^2]$
$q_{Max_{entrainment}}$	maximum heat flux that the heat pipe can reject considering entrainment limitations $[W/m^2]$
$q_{Max_{viscosity}}$	maximum heat flux that the heat pipe can reject considering viscosity limitations $[W/m^2]$
R_{tot}	overall thermal resistance [K/W]
r_b	bubble nucleation site radius [m]
r_c	radius of the condenser section [m]
r_c	radius of the heat pipe container [m]
r_e	radius of the evaporator section [m]
r_h	effective capillarity radius [m]
r_s	radius of nucleated spherical particles [m]
r_w	radius of the wick [m]
$T_{condenser}$	temperature of the working fluid in the condenser section [K]
$T_{evaporator}$	temperature of the working fluid in the evaporator section [K]
$T_{fluid_{boiling}}$	boiling temperature of the working fluid [K]
$T_{fluid_{critical}}$	temperature of the working fluid at its critical point [K]
$T_{fluid_{melting}}$	melting temperature of the working fluid [K]
$t_{support}$	thickness of the heat pipe structural support [m]

Acronyms

ATR	Air Turbo Rocket
CMC	Ceramic Matrix Composite
DMR	Dual Mode Ramjet
EPS	Electrical Power System
FEM	Finite Element Method
FCS	Flight Control Subsystem
ODE	Ordinary Differential Equation
TEMS	Thermal and Energy Management System
TPS	Thermal Protection System
UHTC	Ultra High Temperature Ceramics Coating

heat pipe can be simply described as a self-contained, two-phase heat transfer device which consists of a container, a wick, and a working fluid. At first, the incoming heat is collected at the heat pipe evaporator region; then, the heat is conducted through the container and into the wick/working-fluid matrix, where it is absorbed thanks to the evaporation of the working fluid. The heated vapor flows towards a slightly cooler region of the heat pipe, called condenser, where the working fluid condenses, rejecting the heat previously stored through the wick/working-fluid matrix and container. The heat pipe cycle is completed when the liquid comes back to the heated region (evaporator) making benefit of the capillary pumping action of the wick. During normal operation, heat pipes is characterized by a very high effective thermal conductance, maintaining a nearly uniform temperature over the entire heat-pipe length. As far as high-speed aircraft and space vehicles are concerned, ad-hoc tailored heat pipe arrays may be suitable for integration within wing and air-intake leading edges to transport the high net heat input occurring in proximity of the stagnation point to a cooler region, raising the temperature there above the radiation equilibrium temperature and thus rejecting the heat by radiation [19].

Even if heat-pipe technologies and applications to high-speed transportation have already been thoroughly examined and reported in literature, none of them discloses an integrated conceptual design methodology able to anticipate the effect of heat pipes solution onto the vehicle performance. This paper discloses a methodology implementing

an incremental approach which includes multi-fidelity design, modelling and simulation techniques. The methodology allows to carry out the first estimations of the effectiveness of embedded heat-pipe solutions since the very early design stages, when the first set of Design, Interface and Operational Requirements are elicited, in line with the modern design philosophies [20,21]. Then, the multi-fidelity approach allows for a continuous refinement of the thermal protection system under development, with the possibility to carry out numerical simulations and requirements verification. The development and application of the methodology is crucial to manage the increasing level of integration of future hypersonic systems as well as to deal with the worldwide incentive to dramatically shorten the design and development phases with a limited amount of time and budget resources [22]. Moreover, a new synthetic visualization of the heat pipe design space is suggested. This visualization reports the maximum heat flux rejection capability as a function of the main design parameters, such as for example the wick radius. The performance curves associated to each heat transfer limit (the capillary, entrainment, viscosity, chocking and boiling limits) allow for the identification of feasible areas in the design space.

In addition to the novelty of the multi-fidelity methodology here disclosed, the results of the investigations reveal the importance of in-depth analysing the behaviour of the heat-pipe throughout its operative cycle, especially when liquid metals are used as working fluids and the duration of start-up phase shall not been neglected.

2. Heat pipe integrated conceptual design approach

The multi-fidelity design approach described and applied in this paper can be summarized with the workflow shown in Fig. 1. As clearly indicated, the heat pipe design activities can start as soon as the first operational (see Sec. 2.1), design and interface requirements (see Sec. 2.2) are available. The first heat pipe design and sizing activities consists in the definition of feasible integrated architectures, and selection of the most appropriate working fluids and compatible wick and case materials. The analysis of the heat transfer limits (the capillary, entrainment, viscosity, chocking and boiling limits) is here suggested as guideline for the identification of a suitable design space and rational down-selection of the most promising solution. Following this approach, the identified solution is also characterized by some geometrical characteristics, thus allowing for the integration of a representative heat-pipe mock-up into a full-scale CAD model. This step is a preparatory activity for the following Finite Element Modelling (FEM) analysis (Sec. 3.1). Moreover, the methodology suggests the possibility to verify the effectiveness of the designed and sized integrated heat pipe solution, by means of a numerical code in which the heat pipe arrangement is modelled through electrical analogy (Sec. 4). For the sake of clarity, STRATOFLY MR3 is used as example throughout this publication. However, the methodology has been conceived with a broader validity, ensuring its applicability to a wide range of high-speed vehicles, including for example future reusable access to space vehicles.

2.1. Heat pipe operational requirements

2.1.1. STRATOFLY reference mission

The very first design step of any Thermal Protection System (TPS) shall consist in the identification and analysis of the thermal environment characterizing the aircraft nominal operating scenario. This step is essential to elicit the first list of requirements that will guide the

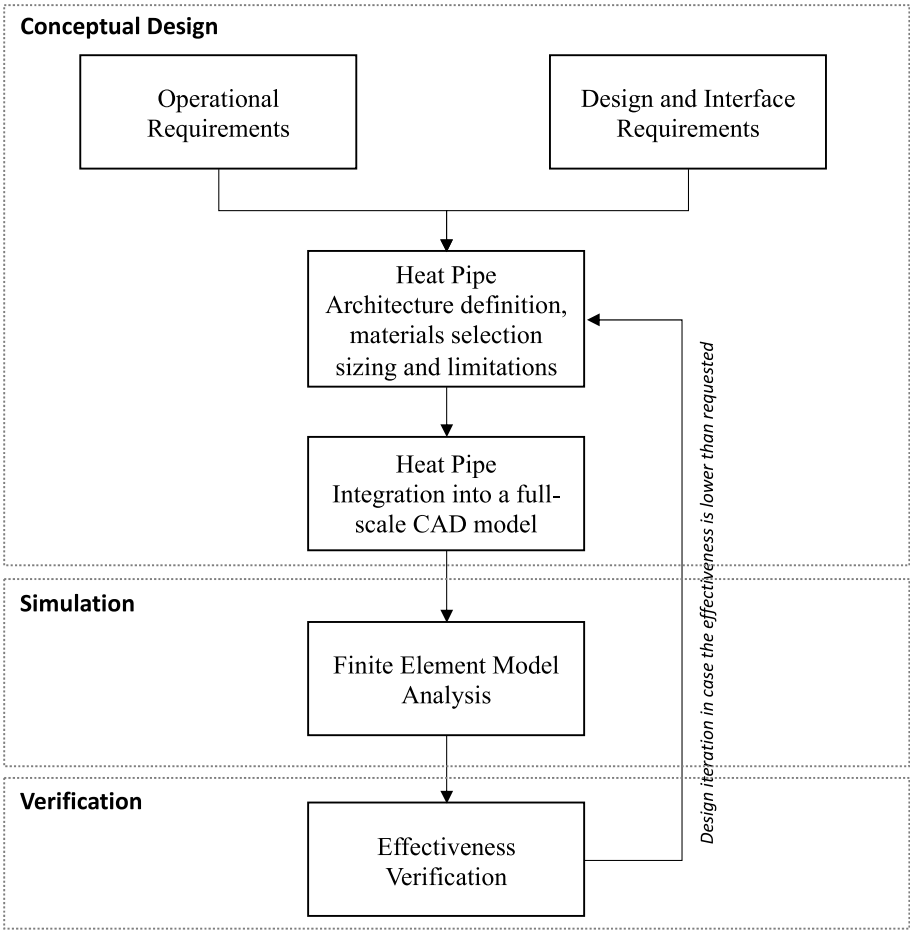

Fig. 1. Design, Analysis and Verification Methodology for an air-intake leading edge heat pipe solution.

designers through the design and sizing of any adopted solution. However, a prerequisite for the characterization of the thermal environment is the identification of a reference nominal trajectory. Specifically looking at STRATOFLY MR3, a Brussels – Sydney (BRU-SYD) trajectory is considered as reference, benefiting of the heritage of previous European projects and, specifically, of the analyses carried out for its predecessor LAPCAT MR2.4 [23].

Recently, additional detailed aerodynamic investigations have been performed, aiming at increasing the accuracy of the aero-propulsive databases and a new set of mission simulations [24] have been carried out to verify the possibility to fulfil the initial set of requirements. As reported in Ref. [24], thanks to in-depth investigations, the complexity of the aerodynamic model has been increased incrementally, from the sole clean external configuration up to the complete one, including propulsion systems elements and flight control surfaces. At each step, the aerodynamic analysis has been complemented with detailed mission analysis, in which the different versions of the aero-dynamic databases have been used as input for the trajectory simulation. However, the trajectory baseline remains unchanged: STRATOFLY MR3 is conceived to fly along long-haul routes reaching Mach 8 during the cruise phase at a stratospheric altitude (h > 30,000 m), carrying 300 passengers as payload. Fig. 2a shows the Reference MR2.4 flight trajectory, while Fig. 2b reports the latest results obtained for the MR3 flight trajectory thanks to the upgraded aero-propulsive database. STRATOFLY MR3 has a waverider configuration with the engines and related air ducts completely embedded into the airframe and located at the top of the vehicle (dorsal mounted configuration). The integration of the propulsive system at the top of the vehicle allows maximization of the available planform area for lift generation without additional drag penalties, thus increasing the aerodynamic efficiency, and it allows optimizing the internal volume. This layout guarantees furthermore to expand the jet to a large exit nozzle area without the need to perturb the external shape which would lead to extra pressure drag. However, this specific airframe-propulsive integration naturally exposes the air-intake leading edges to extreme local temperatures, during different phases of the mission. From the horizontal take-off up to Mach 4–4.5, the MR3 is powered by the six Air-Turbo-Rocket (ATR) engines; then the transition to Dual-Mode-Ramjet (DMR) engine allows for a further acceleration to finally reach cruise conditions (Mach 8 and altitude 32 ÷ 33.8 km). The DMR shutdown is foreseen at the end of the cruise, where a gliding deceleration occurs up to the landing. In Ref. [24], the possibility to perform a powered descend and landing is mentioned but further investigations are needed.

Considering the very limited differences between the simulated trajectories and the fact that the dynamic pressures are always lower than the 50 kPa reached at the beginning of the cruise by the MR2.4, the original MR2.4 flight envelope (in terms of altitudes and Mach numbers) is kept as reference for the MR3 vehicle as well (Fig. 2).

2.1.2. Aero-thermal assessment throughout the trajectory

Once the reference mission is selected, it is possible to verify the vehicle thermal behaviour throughout its trajectory. At this purpose, both engineering formulations, such as the Zoby's model [25], and numerical simulations by means of the Finite Element Methods (FEM) can be exploited, depending on the available input data at the beginning of the analysis. If the aerothermal assessment is carried out at the beginning of the conceptual design, engineering formulations are most suitable. In the present approach, the stagnation-point heat flux is estimated along the flight trajectory by the formulation of Zoby for hot-wall conditions, where a spherical nose of radius R_N is assumed (eq. (1)), whereas total temperature of eq. (2) is used to get the heat transfer coefficient h_0 of eq. (3).

$$\dot{Q}_{zoby} = 3.88 \times 10^{-4} \sqrt{\frac{p_{t,2}}{R_N}} \times (H_0 - h_w) \tag{1}$$

$$T_0 = T_\infty \times \left(1 + \frac{\gamma - 1}{2} M^2\right) \tag{2}$$

$$h_0 = \frac{\dot{Q}_{zoby}}{T_0 - T_w} \tag{3}$$

Please, note that estimating the stagnation-point heat flux for a spherical nose instead of a quasi-2D intake leading edge as the one of MR3 vehicle constitutes an additional degree of conservativity.

By using the CAD model describing the external vehicle layout, a transient thermal analysis has been performed by means of a proper numerical methodology. The procedure adopted for the analysis of the STRATOFLY MR3 vehicle is schematically reported in Fig. 3.

The available CAD model of the vehicle is used to create the numerical model implemented in Ansys Workbench, where the computational mesh is generated. Complementary, a set of stationary CFD simulations have been completed in specific flight conditions to evaluate the convective heat transfer coefficient spatial distribution over the vehicle surface $h(x)|_{CFD_i}$. Ultimately, the reference flight trajectory has been split in a certain number of legs, corresponding to the specific flight conditions previously analysed through stationary CFD. This allows to keep the effect of both angle of attack and Mach number into account. Indeed, each time-leg approximates properly the aerothermal conditions at a specific time instant, in which the exact CFD stationary solution is available, for a certain trajectory time-step. The used CFD-computed aerodynamic and aerothermodynamic coefficients strictly depend on flight parameters, such as Mach number, Reynolds number, angle of attack etc., therefore this approach implicitly considers flight conditions in the heat transfer coefficient estimation.

For each trajectory leg, the heat transfer coefficient distributions are properly scaled by the stagnation-point heat transfer coefficient variation along the selected trajectory leg, normalized with respect to the corresponding reference condition (i.e. the flight condition analysed by

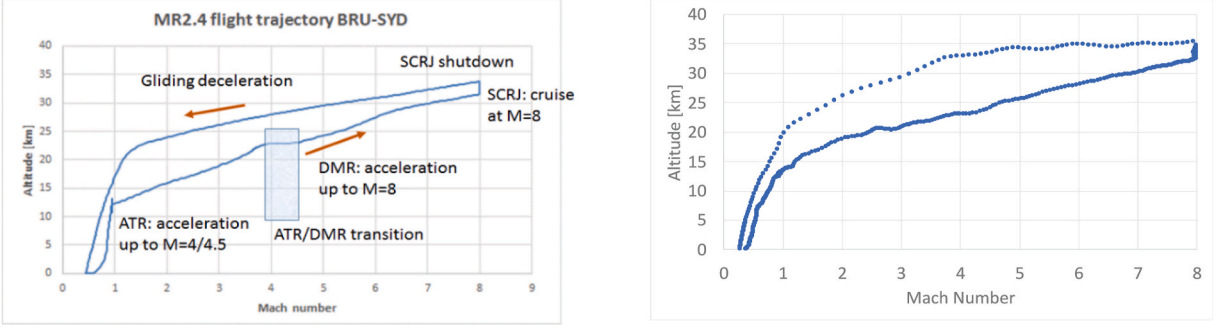

Fig. 2. (a) Reference MR2.4 flight trajectory and (b) MR3 flight trajectory with new aero-propulsive database.

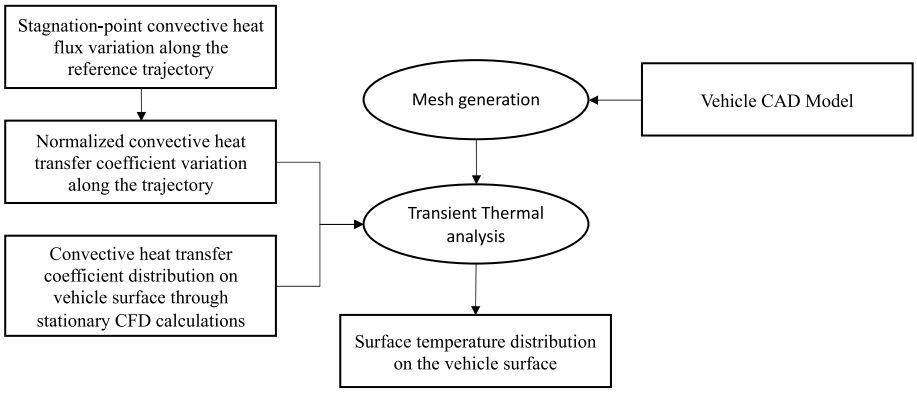

Fig. 3. Transient Thermal Analysis procedure set up for STRATOFLY MR3.

CFD). Referring to the nomenclature reported in Fig. 4, Eq. (4) is applied.

$$h(x,t) = h(x)|_{CFD_i} \cdot \frac{h_0(t)}{h_0(t_{CFD_i})} \tag{4}$$

In particular, the stagnation-point convective heat transfer coefficient h_0 is estimated by scaling the hot wall stagnation-point convective heat flux variation along the trajectory by the difference between the stagnation temperature (T_0) and the wall temperature profile (T_w), as reported in Eq. (3).

For each FEM time instant, the hot wall stagnation-point convective heat flux variation along the trajectory, obtained through this numerical modelling is hereafter compared with the simplified Zoby's formulation. Fig. 5 shows that the total temperature and the heat transfer coefficient at stagnation points from Zoby's calculation and as rebuilt on the FEM are in very good agreement. In particular, Fig. 5 plots respectively the trend of the total temperature and of heat transfer coefficient computed by Zoby's formulation (continuous line), and shows on the same graph the corresponding values, at FEM time instants (star marks), evaluated by eq. (4).

The transient thermal analysis is then set assuming, as convective boundary condition, the heat transfer coefficient evaluated according to the previously discussed procedure and to the stagnation temperature profile (in coherence with the CFD modelling). Please, notice that in addition to the convective heat fluxes, radiative dissipation condition has also been considered for all the external surfaces. Therefore, the overall thermal balance can be written as follows:

$$\dot{q} = h \cdot (T_0 - T_w) - \sigma \cdot \varepsilon \cdot T_w^4 \tag{5}$$

2.2. Heat pipe design and interface requirements

2.2.1. STRATOFLY MR3 vehicle configuration

STRATOFLY MR3 is a highly integrated vehicle, where propulsion, aerothermodynamics, structures and on-board subsystems are strictly interrelated to one another, as highlighted in Fig. 6 [26–28]. Looking inside the aircraft, the use of a bubble structure has successfully demonstrated to achieve lightweight airframe with multi-functional roles, such as passenger cabin, multiple split tanks with anti-slosh baffles, engine bays, intake flow-paths etc., to eventually integrate all subsystems in a harmonious way. Liquid hydrogen has been selected as propellant, thanks to its high specific energy content. The high specific energy of the liquid hydrogen allows the vehicle to cover antipodal routes flying at Mach 8, without emitting any CO_2. In the first part of the project, conceptual design methods and tools have been used to preliminary assess mass, volume and power budgets following a top-down approach. Subsequently, in the second part of the project, those analysis have been verified through the design, sizing, integration and in some cases simulation of each subsystem. To properly account for the mutual relationships which do exist among the subsystems and between each of them and the vehicle structure and mission, the subsystem design was carried out in parallel to the vehicle conceptual design and mission

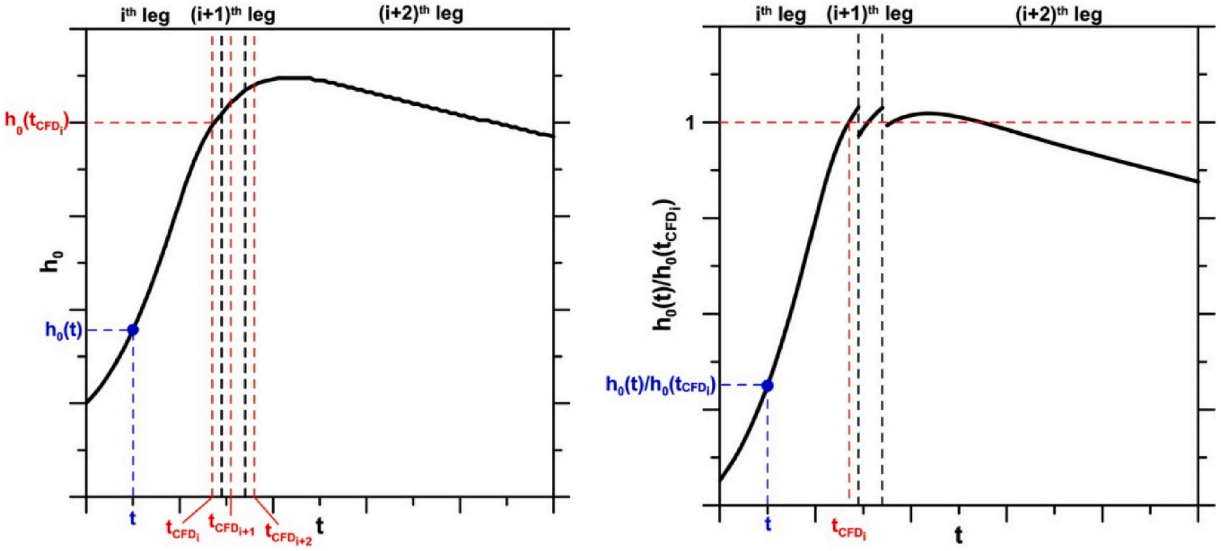

Fig. 4. a) Description of CFD results scaling along the trajectory. b) Typical normalized stagnation-point heat transfer function.

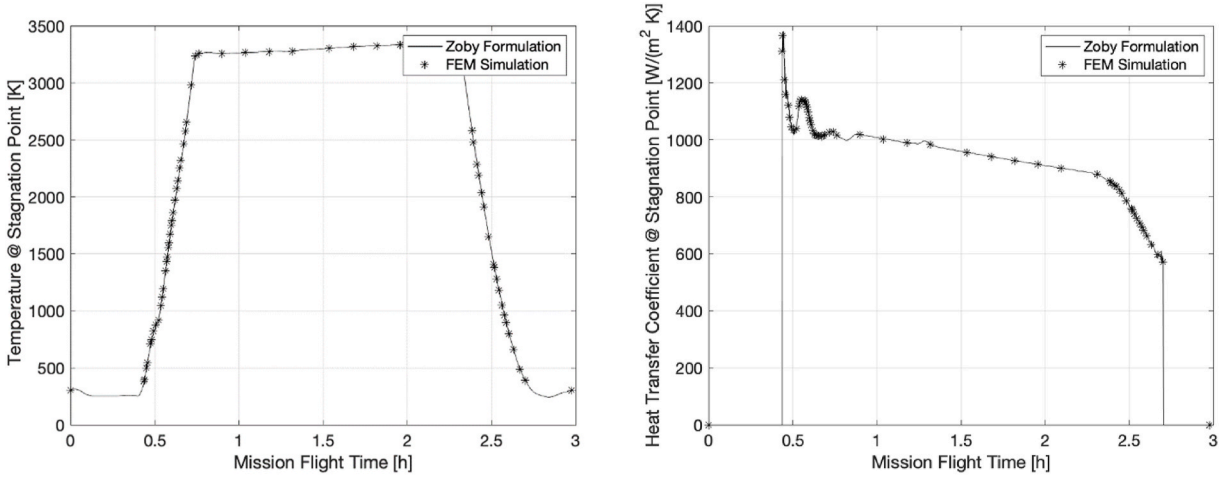

Fig. 5. Stagnation temperature profile and heat transfer coefficient profile according to Zoby w.r.t. the values chosen at FEM transient thermal time instants.

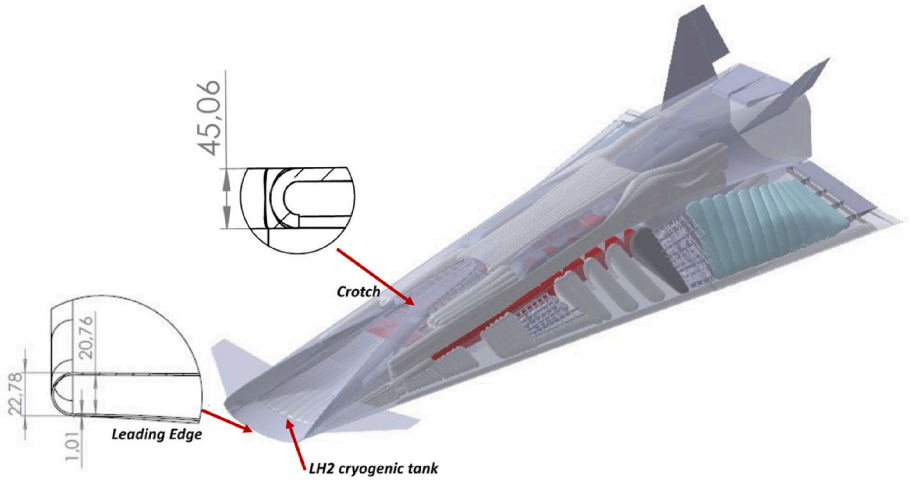

Fig. 6. STRATOFLY MR3 arrangement constraints within the air intake leading edges (measures in mm).

analysis. In details, starting from the mission analysis of the MR3 clean configuration (with no control surfaces activated), preliminary requirements for the propellant subsystems have been elicited and exploited to initialize the subsystem design process, providing the first important guesses about the centre of gravity position and shifts throughout the mission [36]. This outcome has been used to verify the first sizing of the Flight Control Subsystem (FCS) which allowed to refine the trajectory simulations using a complete aerodynamic database (not only the clean one) coupled with stability analysis. In turn, the finalization of the propellant subsystem design has been necessary to complete the design of all the subsystems composing the multidisciplinary Thermal and Energy Management System (TEMS), which integrates Propulsive, Propellant, Thermal Control, Thermal Protection, Electrical and Environmental Control Systems. In the end, in line with the most recent approaches for on-board subsystems (more and all-electric philosophy), the Electrical Power Subsystem (EPS) architecture has been defined, inspired by the most advanced more-electric civil aircraft (Boeing 787). The subsystems have been thoroughly designed, sized and integrated into the 3D CAD model. The integration into the physical model has guaranteed the possibility to carry out structural analysis and optimization as well as the overall aero-thermal assessment of the entire vehicle configuration throughout the mission.

It is worth noticing that the embedded propulsion systems, meant to reach unprecedent performance levels, poses serious challenges for the thermal protection of the frontal part of the vehicle, and specifically of the small-radius air-intake leading edges. Fig. 6 reports the main spatial and volumetric constraints of the air-intake leading edge structure. Both at the lower lip as well as at the crotch of the air intake, very narrow volume is available to host possible Thermal Protection System (TPS) solutions. However, the platelet shape of the leading-edge area as well as its proximity to the foremost cryogenic bubble tanks, which may act as heat sinks, reveals the potential for the adoption of a highly integrated heat pipe solution.

2.3. Heat pipe sizing

Fig. 7 summarizes the heat pipe conceptual design methodology disclosed in this paper. Once the operational and design requirements have been properly identified, including temperature boundaries and heat flux as well as geometrical arrangements, orientation of the pipe and proximity to viable heat sinks, it is then possible to define alternative TPS architectures. Once the problem is characterized, and viable architectural options are sketched, it is possible to identify suitable working fluid and materials for both the wick layers and the container. As indicated into the diagram, the identification of working fluid and of the materials for the different components have mutual influences because of compatibility reasons and operational limitations, both depending on heat pipe architecture too.

It is thus possible to define several criteria that shall be satisfied to guarantee the feasibility of the solution, as listed hereafter:

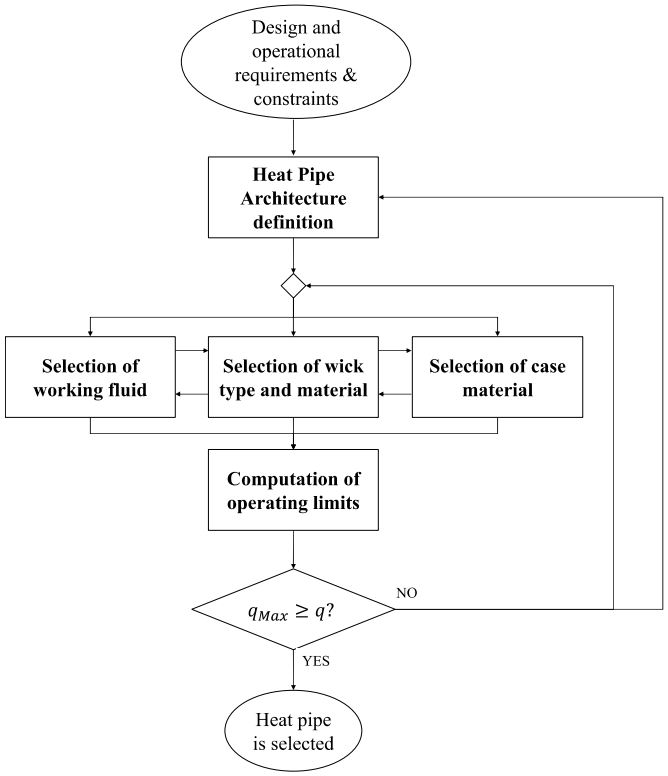

Fig. 7. Heat Pipe sizing process.

1. $T_{fluid_{melting}} < T_{condenser}$ [Req 1]
2. $T_{fluid_{boiling}} < T_{evaporator}$ [Req 2]
3. $T_{fluid_{critical}} > T_{evaporator}$ [Req 3]
4. $p_{fluid_{critical}} > p_{evaporator}$ [Req 4]

As soon as the architecture satisfies all criteria, the heat flux limitations associated to the selected arrangement can be computed.

Particularly, to evaluate the maximum heat flux managed by a specific heat pipe, the model focuses on the computation of:

- $q_{Max\ capillarity}$, the maximum heat flux that can be rejected by the heat pipe considering properties of the fluid, geometrical arrangement and dimension of the heat pipe (in W/m^2);
- $q_{Max\ entrainment}$, the maximum heat flux that can be rejected by the heat pipe considering entrainment phenomena. This basically happens when shear forces applied by vapor on liquid are above the surface tension of the liquid itself, which is captured by vapor flows and sent back to the condenser, without reaching the evaporator (in W/m^2);
- $q_{Max\ vis\cos ity}$, the maximum heat flux that can be rejected by the heat pipe when the pressure drop in the evaporator is so high to prevent the vapor to flow in the condenser (in W/m^2);
- $q_{Max\ chocking}$, the maximum heat flux that can be rejected by the heat pipe when vapor reaches sonic condition (in W/m^2);
- $q_{Max\ boiling}$, the maximum heat flux that can be rejected by the heat pipe avoiding evaporator dry out due to fluid nucleation boiling in the wick (in W/m^2).

The necessary condition for a heat pipe architecture to be validated is then the satisfaction of these additional criteria concerning maximum heat fluxes, as listed hereafter:

5. $q_{Max_{capillarity}} > q_{Max}$ [Req 5.1]
6. $q_{Max_{entrainment}} > q_{Max}$ [Req 5.2]
7. $q_{Max_{viscosity}} > q_{Max}$ [Req 5.3]
8. $q_{Max_{chocking}} > q_{Max}$ [Req 5.4]
9. $q_{Max_{boiling}} > q_{Max}$ [Req 5.5]
10. Container and wick materials shall be compatible with the fluid [Req 6]
11. Heat pipe architecture shall be compatible with geometrical arrangement. Particularly, as far as intake crotch region is concerned, the heat pipes assembly height shall not exceed 45 mm [Req 7]

In the following sections, the analysis of the above-mentioned requirements reveals that it is possible to associate the maximum heat fluxes theoretically manageable by the heat pipe with the main dimensions of the heat pipe itself. The main output of the process is thus a design space relating heat pipe performance, dimensions and geometrical constraints. In case the analysis of the design space reveals the unfeasibility of the analysed alternative, it might be convenient to select a different working fluid or materials layout, as well as to adopt a different heat pipe architecture.

In the following subsections, details on each step of the methodology described in Fig. 7 are reported, highlighting the peculiarities raised by the specific application to the MR3 air-intake leading edge.

2.3.1. Capillarity limitations

The maximum heat flux that can be managed by the heat pipe before encountering capillarity limitations ($q_{Max_{capillarity}}$), i.e., before reaching the condition in which the pipe is no more capable of pumping the fluid within the porous wick, can be expressed as in Eq. (6), using the effective heat pipe length (L_{eff}) and the cross-section area at the evaporator (A_e)

$$q_{Max_{capillarity}} = \frac{q_{capillarity}}{L_{eff} A_e} \tag{6}$$

$q_{capillarity}$, the heat transport capillarity limit in [Wm], can be calculated using Eq. (6), where, σ is the surface tension of the fluid in [N/m] and can be expressed using Eq. (7) and knowing the wicking factor (H_l), the load factor (n), the gravity acceleration (g) and the density of the liquid phase (ρ_l); $\Delta P_\perp$ is the perpendicular hydrostatic pressure drop in $[N/m^2]$ and can be expressed using Eq. (8), knowing density of the liquid phase (ρ_l), the load factor (n), the gravity acceleration (g), the radius of the evaporator section (r_e) and the pipe installation angle (ψ); F_l is the equivalent frictional coefficient for liquid flow in $[m^4/s]$ and can be expressed using Eq. (9), knowing the dynamic viscosity and the density of the liquid phase (μ_l, ρ_L), the wick permeability (K), the wick cross-section (A_w), the latent heat of vaporization (λ); F_v is the equivalent frictional coefficient of the vapor flow in $[m^4/s]$ and can be computed using Eq. (10), knowing the reference friction coefficient (f_{Re}), the dynamic viscosity and the density of the vapor phase (μ_v, ρ_v), the radius and the Area of the evaporator section (r_e, A_e) and the latent heat of vaporization (λ); and K is wick permeability in $[m^2]$ and can be computed using Eq. (12), knowing the effective capillarity radius (r_h) and the reference friction coefficient (f_{Re}).

$$q_{capillarity} = \frac{2\sigma/r_h - \Delta P_\perp - \rho_l n g l_{hp} \sin(\psi)}{F_l + F_v} \tag{7}$$

$$\sigma = H_l n g \rho_l \tag{8}$$

$$\Delta P_\perp = 2\rho_l n g r_e \cos(\psi) \tag{9}$$

$$F_l = \frac{\mu_l}{K A_w \lambda \rho_l} \tag{10}$$

$$F_v = \frac{(f_{Re}\mu_v)}{2 r_e^2 A_e \rho_v \lambda} \tag{11}$$

$$K = \frac{2 r_h}{2 f_{Re}} \tag{12}$$

Moreover, L_{eff} and L_t are the effective and real heat pipe lengths

respectively, in [m], and can be computed following Eq. (13) and Eq. (14), considering the contributions of the condenser, adiabatic and evaporator sections. A_e and A_w are the evaporator and wick cross sections respectively and can be evaluated using Eq. (15) and Eq. (16), knowing the evaporator and the external wick radius.

$$L_{eff} = \frac{1}{2}L_c + L_a + L_e \tag{13}$$

$$l_{hp} = L_c + L_a + L_e \tag{14}$$

$$A_e = \pi r_e^2 \tag{15}$$

$$A_w = \pi r_w^2 \tag{16}$$

2.3.2. Entrainment limitations

The maximum heat flux that can be managed by the heat pipe before encountering entrainment limitations ($q_{Max_{entrainment}}$), i.e., before reaching the condition in which the liquid is captured by vapor flow and sent back to the evaporator since the shear forces applied by vapor on liquid are higher than its surface tension, can be expressed as in Eq. (17).

$$q_{Max_{entrainment}} = A_e \lambda \sqrt{\frac{\sigma \rho_v}{2 r_h}} \tag{17}$$

2.3.3. Viscosity limitations

The maximum heat flux that can be managed by the heat pipe before encountering viscosity limitations ($q_{Max_{viscosity}}$), i.e., before reaching the condition in which the pressure drop in the evaporator is so high to prevent the vapor to flow in the condenser, can be expressed as in Eq. (18). It is a physical phenomenon similar to the capillarity limitation, which is applicable to liquid phase.

$$q_{Max_{viscosity}} = \frac{\pi r_e^4 \lambda \rho_v p_{evaporator}}{12 \mu_v L_{eff}} \tag{18}$$

where p_{ev}, the pressure of vapor in the evaporator, can be computed using the state equation of gas (supposed ideal).

2.3.4. Chocking limitations

The maximum heat flux that can be managed by the heat pipe before encountering chocking limitations ($q_{Max_{chocking}}$), i.e., before reaching the condition in which the vapor flow is sonic, can be expressed as in Eq. (19), where M_v Mach number of vapor flow.

$$q_{Max_{chocking}} = \lambda \rho_v M_v c \tag{19}$$

2.3.5. Boiling limitations

The maximum heat flux that can be managed by the heat pipe before encountering boiling limitations ($q_{Max_{boiling}}$), i.e., before reaching the evaporator dry-out condition, can be expressed as in Eq. (20), where: k_{eff} is the effective liquid/wick conductivity which can be computed using Eq. (21) and knowing the liquid and wick thermal conductivities (k_l, k_w), and the wick conductivity factor (ε); ΔP_c is the capillarity pressure differential between vapor and liquid phases in $\left[\frac{N}{m^2}\right]$, which can be computed using Eq. (22) and knowing the perpendicular hydrostatic pressure drop ($\Delta P_\perp$), the surface tension of the fluid (σ), the effective capillarity radius (r_h), the wicking angle (θ) and the axial hydrostatic pressure drop ($\Delta P_\parallel$) which can be evaluated using Eq. (24) and ε is the wick conductivity factor which can be computed using Eq. (23).

$$q_{Max_{boiling}} = \frac{2\pi L_e k_{eff} T_{evaporator}}{\lambda \rho_v \log\left(\frac{r_w}{r_e}\right)} \left(\frac{2\sigma}{r_b} - \Delta P_c\right) \tag{20}$$

$$k_{eff} = \frac{k_l k_w}{\varepsilon k_w + k_l(1-\varepsilon)} \tag{21}$$

$$\Delta P_c = \frac{2\sigma}{r_h}\cos(\theta) + \Delta P_\perp + \Delta P_\parallel \tag{22}$$

$$\Delta P_\parallel = \rho_l n g l_{hp} \sin(\psi) \tag{23}$$

$$\varepsilon = \left(\frac{\pi\left(1 - \left(\frac{r_c}{r_s}\right)^2\right)\left(2 - \sqrt{\left(1 - \left(\frac{r_c}{r_s}\right)^2\right)}\right)}{6\left(1 - \left(\frac{r_c}{r_s}\right)^2\right)^{\frac{2}{3}}} \right) \tag{24}$$

2.3.6. Architecture definition

Once the operational and design requirements have been properly identified, including temperature boundaries and heat flux as well as geometrical arrangement, orientation of the pipe and proximity to viable heat sinks, it is then possible to define alternative architectures. In literature, both traditional and innovative architectures have been thoroughly theoretically investigated for aerospace application. However, few architectures have been analysed and tested for hypersonic applications. The typical sizing procedure described in literature has been used to derive proper heat pipes architecture candidates. Considering the volumetric constraints imposed by the peculiar design of the embedded air-intake of the MR3, a dedicated heat-pipe architecture, inspired by the NASP project, has been developed. This architecture has been suggested for both the lower lip as well as for the crotch air-intakes. In both cases, the proximity of the foremost cryogenic tanks suggests a longitudinal orientation of the pipes, parallel to the longitudinal axis of the vehicle. The 22 mm radius of the air-intake leading edges allows to adopt a dual-channel architecture instead of a more traditional tubular architecture. The proposed solution increases the exposed area of the evaporator, thus potentially increasing the heat transfer capability. As schematically reported in Fig. 8, the suggested heat pipe solution is completely integrated into the air-intake structure, assuming that the heat pipe case is perfectly bonded with the panels of the aircraft skin. Eventually, a perfect bonding is also ensured between the case and the wick. Finally, it is worth noting that the rearrest part of the condenser region shall be properly interfaced with the tank external structure, to guarantee the required heat rejection. According to the layout of the tanks, their interface with the pipes assembly and the property of the hydrogen stored in their compartments, it is supposed that the heat

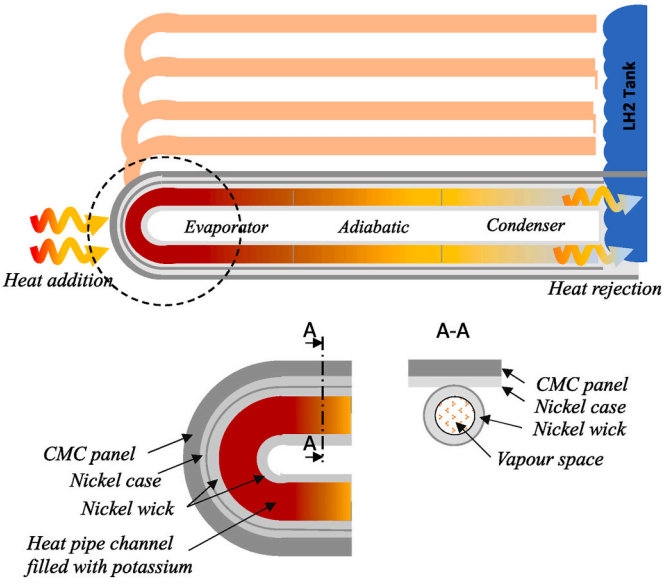

Fig. 8. Overall heat pipe arrangement for the selected case study.

exchange at the condenser is enough to guarantee the correct working cycle of the driving fluid. For this reason, the pipes design is focused on the evaporator side.

2.3.7. Material and design alternatives

As far as the hot structure is concerned, as reported in Refs. [13–15], CMC materials can be widely used for the main structure of hypersonic vehicles such as STRATOFLY MR3. CMC materials can also be employed for specific areas of the vehicle such as the intakes, wing and vertical tail leading edges if the local heat flux does not exceed 0.7 MW/m2. Complementary, for very restricted areas, like the crotch and the lower lip areas of the air-intakes, an alternative solution, able to withstand the higher expected thermal loads, can be represented by tungsten coated by UHTC (Ultra High Temperature Ceramics Coating). The possibility to couple high-temperature materials such as CMC and Tungsten with additional cooling strategies, like the integration of heat pipes, may represent an appropriate solution for the thermal challenges.

More complex is the definition of the materials to be adopted for the wick and the case. Considering the very demanding thermal environment in which hypersonic aircraft operate, only liquid metals may be indicated to act as fluids. Of course, as thoroughly investigated and reported in literature, the adoption of liquid metals heat pipe technology requires dedicated off-design performance analysis, especially looking at minimizing the issues related to the start-up phase.

In Table 1, the reader can find the results of the investigation of different fluid and wick materials for the heat pipe architecture suggested in Fig. 8. Results are shown for the intake crotch region, considering a maximum heat flux of 0.7 MW/m2 to be in line with the constraints of CMC skin. This is a lower value with reference to the average heat flux predicted in Section 2.1.2 (around 0.9 MW/m2, excluding the peak) but proper coatings can be included to raise maximum heat flux capabilities of the skin. Moreover, the analysis reported in Section 2.1.2 is expected to be extremely conservative due to the simplicity of the model. For these reasons, the value adopted as reference is still considered acceptable for the design and trade-off process.

Steel-Mercury and Tungsten Lithium solutions do not meet performance criteria. Titanium-Caesium, Nickel Potassium and Inconel Sodium meet performance criteria, even if they use fluids that are potentially corrosive and flammable. Notably:

- (Ti–Cs) requires $l_{hp} \geq 6m$ to withstand boiling limitation and $r_w > 8.5e-3$ to meet viscous limit. Moreover, $t_{skin\,stagnation} \geq 0.04m$ to allow compatibility with thermal environment. It has capillarity limitations ($\psi = 0°$);
- (Ni–K) requires $l_{hp} \geq 5m$ to withstand boiling limitation and $r_w > 8.0e-3m$ to meet viscous limit. Interface temperature is flexible. Some capillarity limitations are present ($\psi < 1°$);
- (Inconel® - Na) requires $l_{hp} \geq 2m$ to withstand boiling limitation and $r_w > 8.8e-3m$ to meet viscous limit. To reach the required heat transport capability with reduced dimensions, $t_{skin\,stagnation} \leq 0.02m$ with $\psi < 4°$. Geometrical arrangement can be also traded for higher ψ angles.

Therefore, (Ni–K) is the most compact solution and represents the best compromise between thermal environment and start-up problems. It allows double walls installation (solution depicted in Fig. 8), which results to be capable of withstanding and managing the heat flux generated by the identified thermal environment. In this case, Potassium (K) has been considered as driving fluid and Nickel (Ni) is selected as

Table 1
Candidates-criteria matrix summarizing feasible arrangements.

	Steel – Mercury (Hg)	Titanium – Caesium (Cs)	Nickel – Potassium (K)	Inconel® – Sodium (Na)	Tungsten – Lithium (Li)
Req. 1	$T_{condenser} > 235\ K$ *feasible*	$T_{condenser} > 302\ K$ *feasible** *Start-up problem may occur	$T_{condenser} > 337\ K$ *feasible** *Start-up problem may occur	$T_{condenser} > 372\ K$ *feasible** *Start-up problem may occur	$T_{condenser} > 454\ K$ *feasible** *Start-up problem may occur
Req. 2	$T_{evaporator} \gg 630\ K$ *verified*	$T_{evaporator} > 943\ K$ *verified*	$T_{evaporator} > 1032\ K$ *verified*	$T_{evaporator} > 1152\ K$ *verified*	$T_{evaporator} > 1615\ K$ *verified*
Req. 3	$T_{evaporator} < 1763\ K$ *verified*	$T_{evaporator} < 2050\ K$ *verified*	$T_{evaporator} < 2250\ K$ *verified*	$T_{evaporator} < 2500\ K$ *verified*	$T_{evaporator} < 3800\ K$ *verified*
Req. 4	$p_{evaporator} \ll 1510e5\frac{N}{m^2}$ *verified*	$p_{evaporator} \ll 117e5\frac{N}{m^2}$ *verified*	$p_{evaporator} \ll 160e5\frac{N}{m^2}$ *verified*	$p_{evaporator} \ll 370e5\frac{N}{m^2}$ *verified*	$p_{evaporator} \ll 970e5\frac{N}{m^2}$ *verified*
Req. 5.1	*verified*	*verified*	*verified*	*verified*	*verified*
Req. 5.2	*verified*	*verified*	*verified*	*verified*	*verified*
Req. 5.3	*verified*	*verified*	*verified*	*verified*	**Not verified**
Req. 5.4	*verified*	*verified*	*verified*	*verified*	*verified*
Req. 5.5	This is satisfied only for $t_{skin_{stagnation}} > 0.1\ m$, $\psi = 0°$, $l_{hp} \gg 1\ m$, and very low nucleation radius ($r_s \cong 1e-8\ m$) **Critical**	$r_w > 8.50e-3\ m$, $\psi = 0°$ $t_{skin_{stag}} \geq 0.04\ m$ *verified*	$r_w > 8.0e-3\ m$ $\psi \leq 1°$ $t_{skin_{stag}} \geq 0.03\ m$ *verified*	$r_w > 8.80e-3\ m$ $\psi \leq 4°$ $t_{skin_{stag}} \geq 0.02\ m$ *verified*	**Simultaneous satisfaction for $q_{viscosity}$ and $q_{boiling}$ is not possible with considered thermal and geometrical constraints.**
Req. 6	Only Stainless Steel guarantees compatibility with mercury. **Critical**	*verified*	*verified*	*verified*	*verified*
Req. 7	$t_{skin_{stagn}} > 0.1\ m$ $l_{hp} \gg 1\ m$ **Geometrical constraints cannot be not respected.**	$\boldsymbol{t_{skin_{stagn}} > 0.04\ m}$ $\boldsymbol{l_{hp} \geq 6\ m}$ *Not verified for the arrangement specified in Figure 8*	$\boldsymbol{t_{skin_{stagn}} > 0.03\ m}$ $\boldsymbol{l_{hp} \geq 5\ m}$ *Verified for the arrangement specified in Figure 8*	$\boldsymbol{t_{skin_{stagn}} > 0.02\ m}$ $\boldsymbol{l_{hp} \geq 2\ m}$ *Not verified for the arrangement specified in Figure 8*	**Not verified**

material for both primary structure (container) and wick of the heat pipe because of fluid compatibility.

The possibility of replacing Nickel (Ni) with other materials such as Aluminium (Al), Steel, Iron (Fe), Copper (Cu) or Tungsten (W) was not assessed since no results were found on compatibility verification. Titanium (Ti) is instead incompatible with Potassium (K).

Fig. 9 summarizes the results achieved so far for the preliminary design of the air-intake heat-pipe. It shows the main design requirements and design space for the selected architecture. In general, the main design requirements are associated to the thermal environment that the heat pipe shall face, in terms of temperature boundaries and heat fluxes, but they can include also geometrical arrangement as well as orientation of the pipe.

2.3.8. Nickel–Potassium heat pipe characterization

Once the working fluid and wick material have been selected, it is important to analyse their physical properties, to better understand the behaviour of the heat pipe arrangement throughout its operative cycle. The trends reported in Fig. 10 have been considered for the definition of fluid and vapor densities (in kg/m^3) as function of the temperature [37]. Specifically, the interpolation suggests a value of 827 kg/m^3 for Liquid Potassium (K) at around 340 K and 2.08 kg/m^3 for vapor Potassium (K) at around 1420 K. The thermal conductivity (in W/mK) of the fluid as function of the temperature is shown in Fig. 10c.

The wick is considered homogeneous and characterized by a single layer architecture (crown cap).

The same material has been used for both container and wick, i.e. Nickel (Ni). Similar properties are then assumed for both layers. However, since the wick is intrinsically wetted by liquid, the effective thermal conductivity is different if compared to container one. Notably: the container material density $\rho_{cont} = 8900 \frac{kg}{m^3}$, Container thermal conductivity $k_{cont} = 77 \frac{W}{mK}$, Container material specific heat at constant pressure $c_{Pcont} = 440 \frac{J}{kgK}$, Wick material density $\rho_w = 8900 \frac{kg}{m^3}$, Wick thermal conductivity $k_w = 62 \frac{W}{mK}$, Wick material specific heat at constant pressure $c_{Pw} = 440 \frac{J}{kgK}$. Thermal conductivities are derived considering material properties, typical heat pipes arrangements and operating conditions for the specific case study analysed in the paper.

In addition, considering the data available in literature, the evaporation is assumed to occur within 0.7 m from the heat pipe leading edge considering $l_{hp} = 2.78\ m$ (25% of l_{hp}). Similarly, the condensation may occur no earlier than 1.7 m from the heat pipe leading edge considering $l_{hp} = 2.78\ m$ (around 75% of l_{hp}). Effective length and parametrization of both evaporator and condenser areas are computed following some relevant examples from NASP Program, where liquid metal heat pipes have been already studied for similar operating conditions [39].

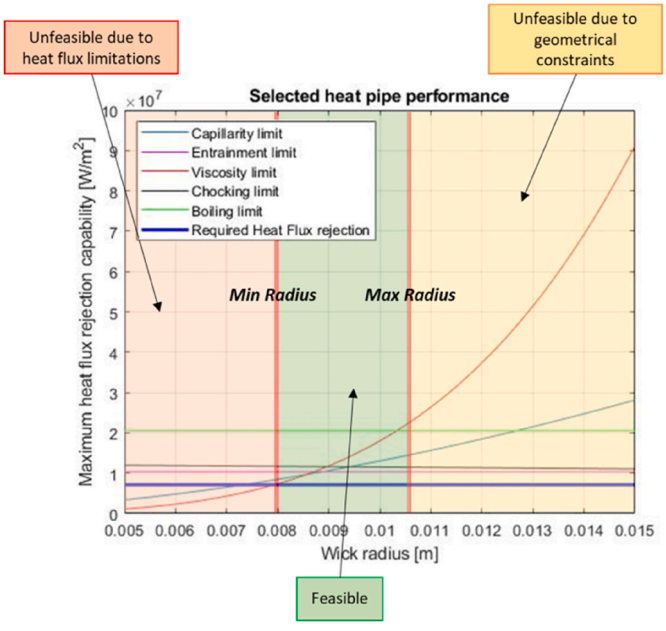

Fig. 9. Synthetic Visualization of the design space for the selected heat pipe architecture and constraints.

Complementary, in view of the main geometrical and constraints, the following geometrical details have been defined, with reference to the variables depicted in Figure XX: radius of the evaporator $r_e = 0.004\ m$, radius of the wick $r_w = 0.008\ m$, radius of the container (case), $r_{cont} = 0.009\ m$, overall heat pipe length $l_{hp} = 2.78\ m$ (as preliminary assumption, the implementation of dedicated ducts bringing the propellant from the tank towards the heat pipes assembly is envisaged to reduce the overall pack length, even if a higher extension was previously considered within the constraints) as well as length and thicknesses of the structural supports $l_{support} \cong 2r_w$, $t_{support} \cong 0.001\ m$ or less (support is required to sustain the heat pipe, which is constrained to the internal wall of the airfoil, even if a detailed design for this component is not included in this paper).

In addition, a skin thickness of 0.02 m close to the stagnation point is assumed and the spacing between the different heat pipe modules is supposed to be equal to $2r_{cont}$. Considering the dimensions of the heat pipes and their spacing, the integration in the crotch region of the MR3 air intake leading edge consists of 74 heat pipe modules.

3. Heat pipe numerical model and simulation

3.1. FEM model

Starting from the design presented in section 2, only a portion of the crotch, corresponding to three pipes width on spanwise direction (Fig. 11), has been modelled. Several finite element models have been developed to perform a parametric study aimed, on the one hand, at evaluating the pipe performance and, on the other hand, at optimizing the air intake layout in terms of material and geometric thicknesses [29–31]. In particular, different materials have been considered for the crotch leading edge (tungsten; titanium; three different types of CMC) and different internal leading-edge thicknesses ranging from 1 to 5 cm have been considered. In order, to perform fast calculations, heat pipes are not included in this FEM, but their effect has been included as subtractive heat flux, i.e. as the heat soaked in by the heat pipe from the leading edge and lateral surfaces. A mesh convergence analysis led to a 3D finite element model of about 5000 nodes and 1000 HEXA solid elements with an average element quality of 0.95 (see Fig. 12).

The following general boundary conditions have been considered (Fig. 13):

- Convective heat fluxes (Eq. (4)) on external wet areas;
- Radiation to ambient for external surfaces;
- Adiabatic wall at cut surfaces location;
- Subtractive heat flux applied at leading-edge internal additional part/heat pipe interface;

3.1.1. Simulation of the heat pipe in a tungsten with high emissivity paint leading edge

A first thermal analysis has been performed by considering a Tungsten crotch leading edge cooled by heat pipes and coated by high emissivity paint ($\varepsilon = 0.8$), using the arrangement reported in Fig. 11. Considering the results of the simplified and stationary evaluation of the heat-pipe effectiveness, a representative subtractive heat flux, computed either through empiric formulation or via ANSYS multi-objective optimization tool, with a peak of about 1 MW/m2, has been chosen and used as input (see Fig. 14). Fig. 14 also shows the temperature map at

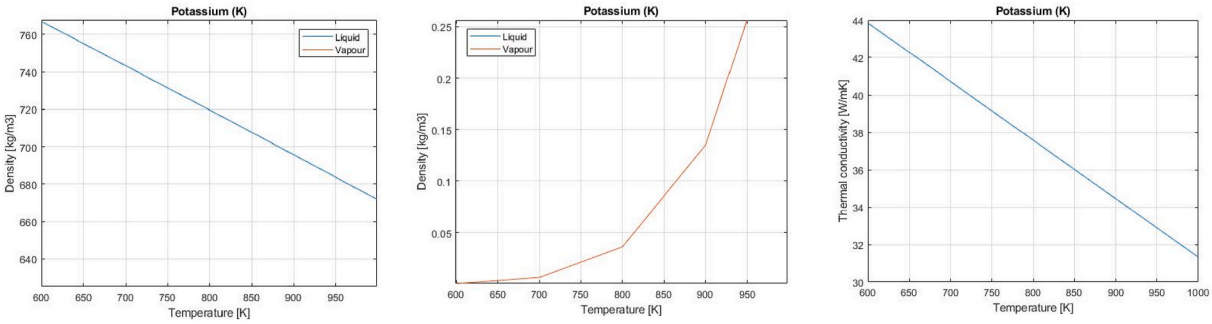

Fig. 10. Potassium density (liquid (a) and vapor (b)) as well as thermal conductivity (c) as function of temperature.

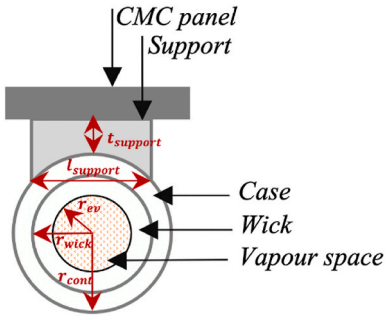

Fig. 11. Cross-section layout of the heat pipe for the selected architecture (upper pipe, not to scale).

maximum time instant, reaching a peak of 1319 °C which is expected to happen at 3242s, that is below the material maximum operative temperature (1800 °C). The comparison of the thermal evolution on the leeward and windward side CMC panels is shown as well on the same plot. Please, notice that the resulting surface temperatures are always widely below the maximum operative temperature of 1600 °C, thus the reference design would be safe.

3.1.2. Simulation of the heat pipe in a tungsten with standard emissivity leading edge

A second thermal analysis has been performed by considering the same heat pipe arrangement, but with a tungsten leading edge not coated by high emissivity paint i.e with its standard emissivity value of about 0.6. Considering that the heat-pipe arrangement is not changing, the same subtractive heat flux has been considered. Fig. 15 shows the temperature map at maximum time instant reaching a peak of 1379 °C at 3094s that is widely below the maximum operative temperature (1800 °C). Moreover, Fig. 13 shows the maximum temperature evolution at crotch with reference to emissivity. Both cases are safe as shown by the thermal evolution on the leeward side and windward side CMC

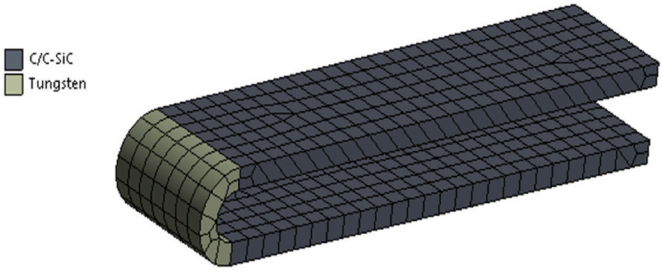

Fig. 13. Crotch 3D mesh.

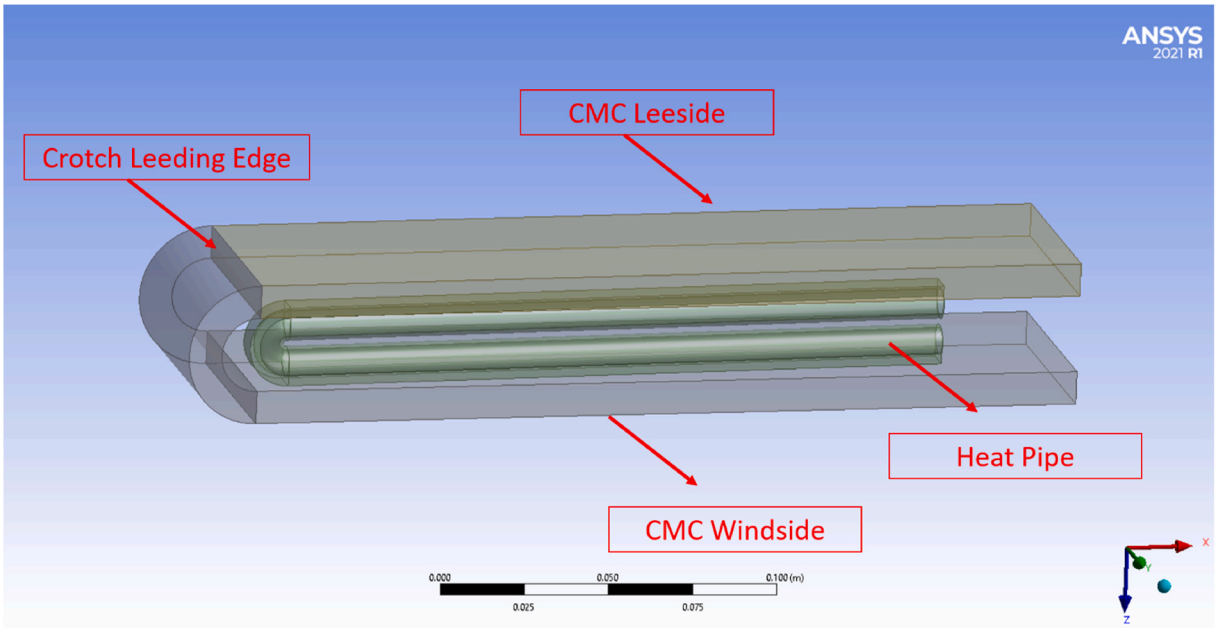

Fig. 12. Crotch geometry generic layout.

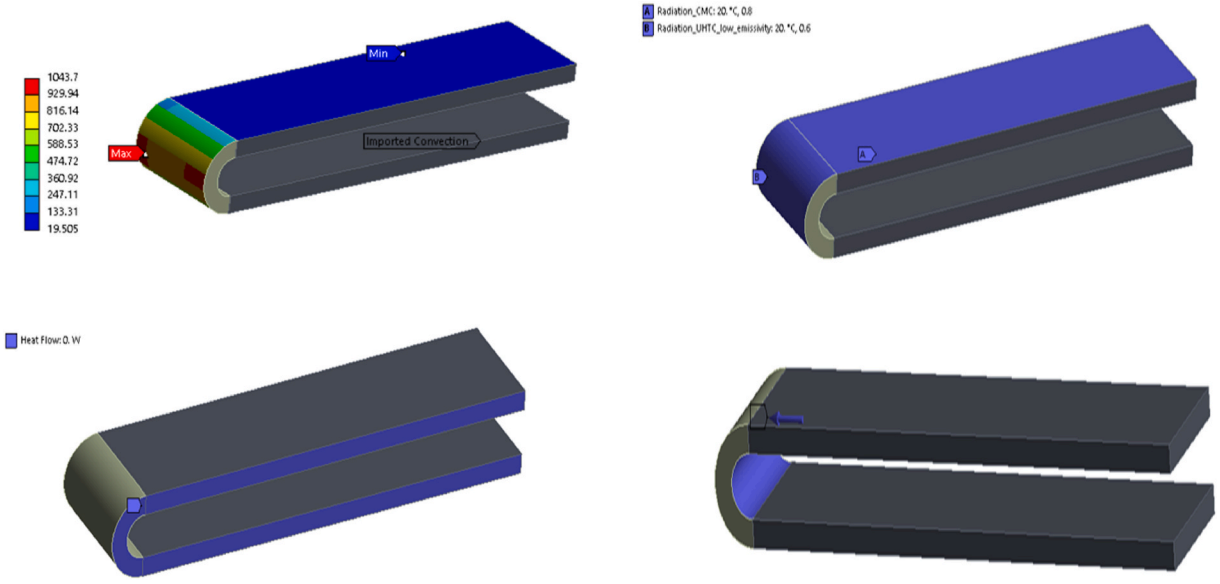

Fig. 14. FEM boundary conditions.

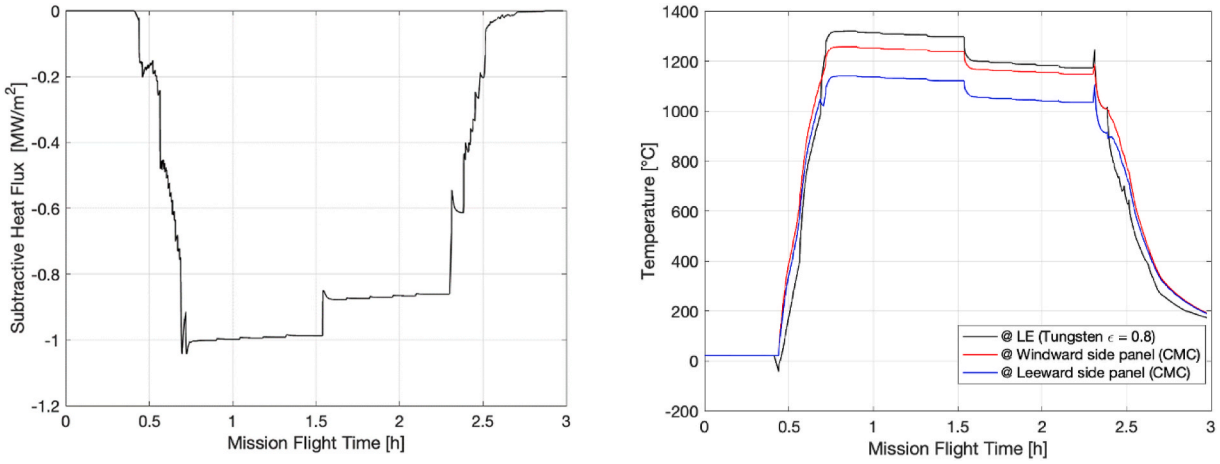

Fig. 15. (a) Subtractive Heat Flux evolution (b) Maximum temperature evolution at crotch leading edge and on CMC panels.

panels with respect to emissivity. Temperature are always widely below the maximum CMC operative temperature of 1600 °C, so this design would be safe as well.

3.1.3. *Simulation of the heat pipe in full CMC leading edge*

A third set of thermal analyses has been performed by considering a full CMC leading edge cooled by heat pipes (same geometrical arrangement as before). Firstly, four different simulations have been performed varying the subtractive heat fluxes from the pipe. This allows checking the effect on maximum temperature on the crotch. Fig. 16 shows the different fluxes whose peaks range from 700 kW/m2 for run 1 to about 950 kW/m2 for run 4. Fig. 16 shows also the corresponding results in terms of maximum temperature on the crotch. It is clear that CMC acts as a very effective thermal barrier. Indeed, an increment in subtractive heat fluxes of the 25%, results in a 4.85% temperature reduction. Finally, run 4 conditions are retained because this scenario keeps the CMC temperature under the theorical service operative temperature fixed at 1600 °C. Fig. 17 shows the thermal map on CMC leading edge at maximum time instant. The temperature reaches, in this case, a peak value of 1598 °C at 2634s. Fig. 17 shows also the thermal behaviour of the CMC panels.

Table 2 compares the maximum temperatures reached on the crotch with respect to the maximum allowable temperature which depends on the selected material. Moreover, considering that Tungsten has a gravimetric density of about 20 g/cm^3 while CMC may reach 2 g/cm^3, the optimized solution for the crotch design appears to consist in a main structure made of CMC (high emissivity ($\varepsilon = 0.8$)), with an integrated heat pipe able to provide a subtractive heat flux with a peak of about 0.9 MW/m and an average of 0.7 MW/m. Furthermore, having a hot interface between tungsten and CMC would lead the designers to look for challenging structural solutions able to guarantee the interface integrity. This solution could appear risky because, apparently, no margins are applied on temperature. Nonetheless, severe uncertainty margin of about 30% are applied on heat fluxes, i.e., on the input of transient thermal analysis. This justifies the selection of CMC as baseline.

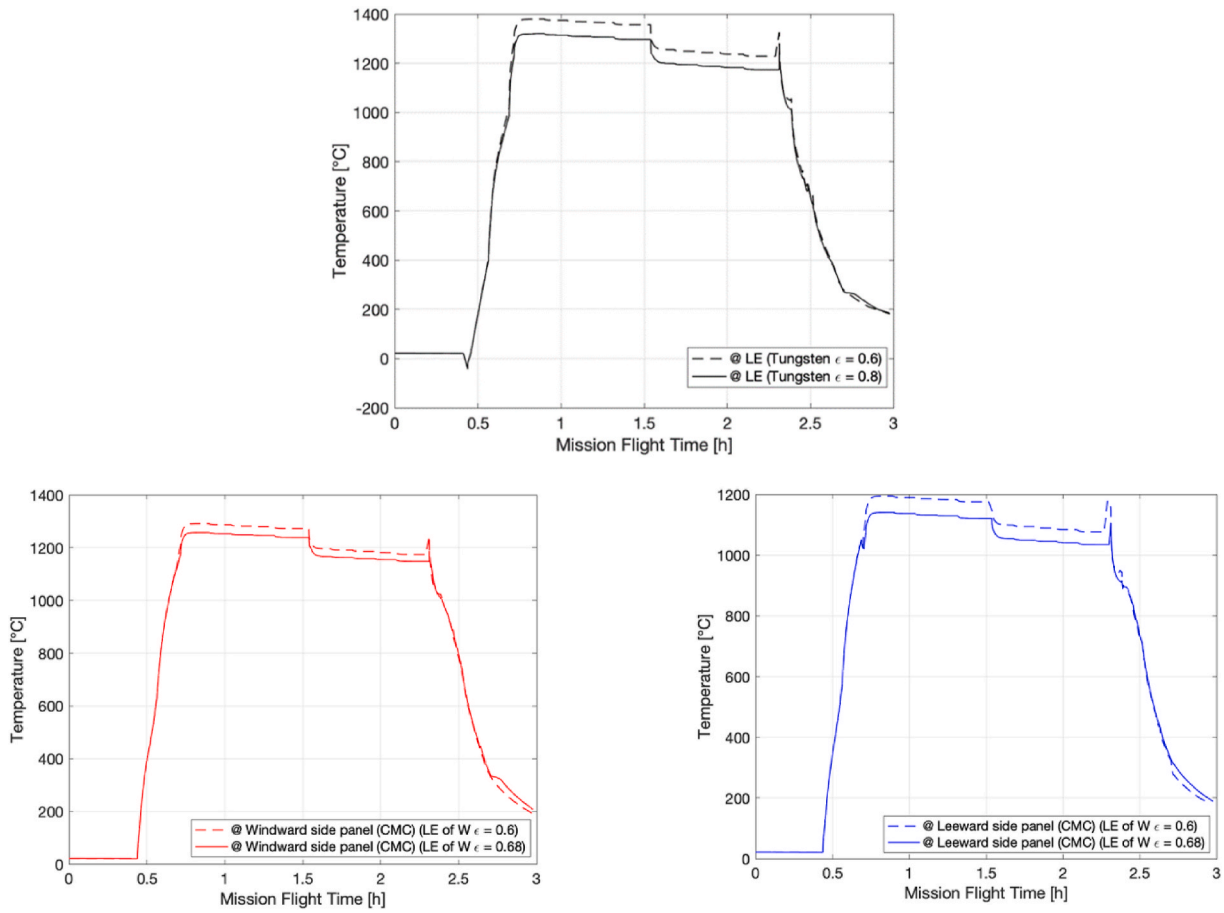

Fig. 16. (a) Maximum temperature evolution at crotch w.r.t emissivity; (b) Maximum temperature evolution at CMC leeward side panel w.r.t emissivity; (c) Maximum temperature evolution at CMC windward side panel w.r.t emissivity.

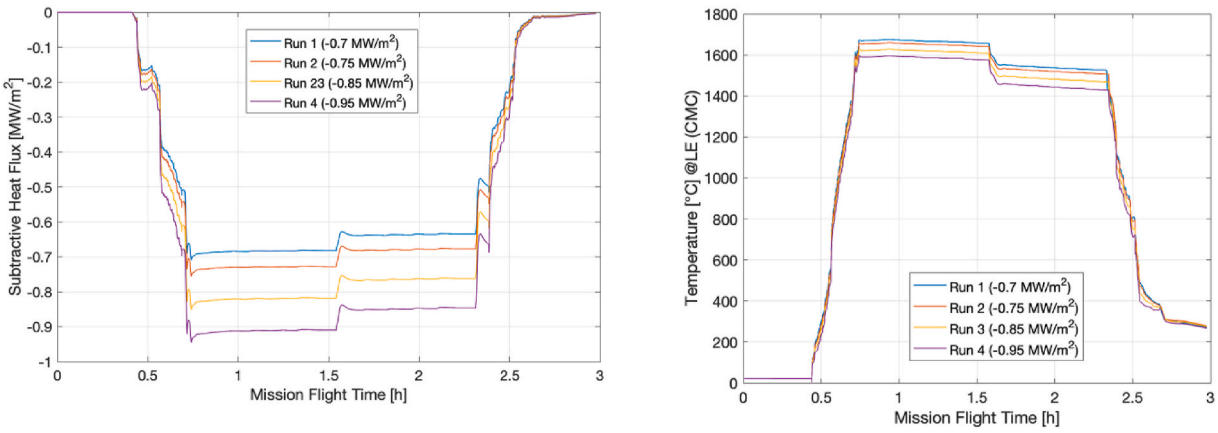

Fig. 17. (a) Subtractive heat fluxes from heat pipe; (b)Maximum temperature evolution at CMC crotch w.r.t different subtractive heat fluxes.

Table 2
Temperature results for different material arrangements.

	Tungsten + High Emissivity Paint	Tungsten + Low Emissivity Paint	CMC
T_{max}	1319 °C	1379 °C	1598 °C
$T_{allowable}$	1800 °C	1800 °C	1600 °C
Safety Margin	27%	23%	0,13%

4. Thermal design verification: heat pipe effectiveness

In order to verify the effective subtractive heat flux guaranteed by the selected heat pipe arrangement, a surrogate numerical code, including the pipes entirely (skin, container and wick) and fluids, as designed in section 2, has been set up. The heat pipe operations can be described by a lumped parametric model based on the electrical analogy [34–36]. Solid components and fluid domains are subdivided into finite sub-volumes, called nodes or lumps. Thermal properties and average temperature of each sub-volume are assumed to be concentrated in the

relative node. Nodes are connected to each other by means of resistive, capacitive and inductive elements modelling different physical phenomena namely thermal or flow resistance, thermal inertia or fluid inertia. Therefore, through the electrical analogy, the heat pipe physical system is reduced to an electrical network where the current and the electric potential represent respectively the thermal flux and the temperature difference between two nodes. Applying Ohm's law and Kirchhoff's, an Ordinary Differential Equation (ODE) can be written per each node, thus reducing the overall transient problem to a simpler linear ODE system.

In nominal conditions, the overall heat transfer rate of the heat pipe (Q) can be described using Eq. (26), where ΔT is the overall temperature difference between the heat source and the heat sink and R_{tot} is the idealized thermal resistance network shown in Fig. 18.

$$Q = \frac{\Delta T}{R_{tot}} \tag{26}$$

The total resistance of the heat pipe R_{tot} is a combination of series and parallel resistances.

However, considering that the thermal resistances of the vapor space is extremely small, in the range of 10^{-8} K/W, the total thermal resistance of the heat pipe can be considered strongly dependent from the conduction resistance of the heat pipe wall in the radial direction.

Following these simplifications, the total power transported by the heat pipe can be defined as in Eq. (27)

$$Q = \frac{K_{eff} * A_{hp} * \Delta T}{L_{eff}} \tag{27}$$

where K_{eff} is the effective thermal conductivity [W/m.K], L_{eff} is the effective length [m], A_{hp} is the cross-sectional area [m^2].

The heat pipe model through the electrical analogy has been implemented in a numerical code, which allows performing a transient thermal analysis using the Mechanical APDL language, integrated in the software ANSYS. The analysis has been conducted taking into account the "effective" thermal conductance of the pipe system, which is changed iteratively.

The simulated heat pipe arrangement is the Nickel–Potassium liquid metal heat pipe. Up until the fluid temperature reaches the potassium boiling temperature (of about 1032*K*), the dominant heat transport mechanism is the conduction through pipe structure. Then, the heat pipe is activated and convection becomes the dominant heat transport mechanism. However, considering that heat pipes are two-phase heat transfer devices, they cannot be characterized by constant thermal conductivities, like solid materials, and an effective thermal conductivity shall be considered. The equation used to calculate the effective thermal conductivity for a heat pipe is reported in (28)

$$K_{eff} = \frac{Q * L_{eff}}{A_{hp} * \left(T_{evaporator} - T_{condenser}\right)} \tag{28}$$

The numerical code simulates the convection phenomenon as an equivalent conduction through pipe structure, where the thermal conductivity of the overall heat pipe is calculated by Eq. (28). When the heat pipe is active, its thermal conductivity typically ranges from 10,000 to 100,000 W/m K, that is 250–500 times the thermal conductivity of solid copper and aluminium, respectively. Fig. 19 shows the flowchart of APDL code.

Numerical code performs a transient thermal analysis consisting of n-step. Two temperature control points have been set: the first is inside the evaporator zone (Fig. 20), the second is located just at the beginning of the condenser zone (Fig. 21). A third control point is placed on the contact surface between the pipe and the internal part of the leading edge (see Fig. 22).

During the analysis the code retrieves the heat flux value (Q) at the interface Heat Pipe-Internal Crotch, the temperature in the evaporator and condenser zone ($T_{evaporator}, T_{condenser}$) at every simulation step. A check on the temperature in evaporator zone at each step is performed and if $T_{evaporator}$ is higher than the boiling temperature of Potassium, K_{eff} can be estimated using Eq. (27), using the $T_{condenser}$ and Q associated to the current step. Once the K_{eff} is evaluated, the conductivity of each material is updated accordingly.

4.1. Verification of the selected TPS air-intake configuration

The numerical model set up to verify the effectiveness of the heat pipe has been applied to all the case-studies previously described (CMC, Tungsten with low and high emissivity painting). Hereafter, the results achieved for the most promising configuration, i.e. the one exploiting CMC at high-emissivity painting for the entire leading edge, are here discussed. Fig. 23a show the results in terms of maximum temperature on the CMC leading edge without heat-pipe activation (black line) and with pipe heat transfer cooling effect, computed by the numerical model (red line). The temperature reaches values of 1830 °C when the analysis is carried out without considering the pipe heat transfer cooling effect, instead 1662 °C is reached when pipe activation is considered. Complementary, Fig. 23b shows also the corresponding results in terms of

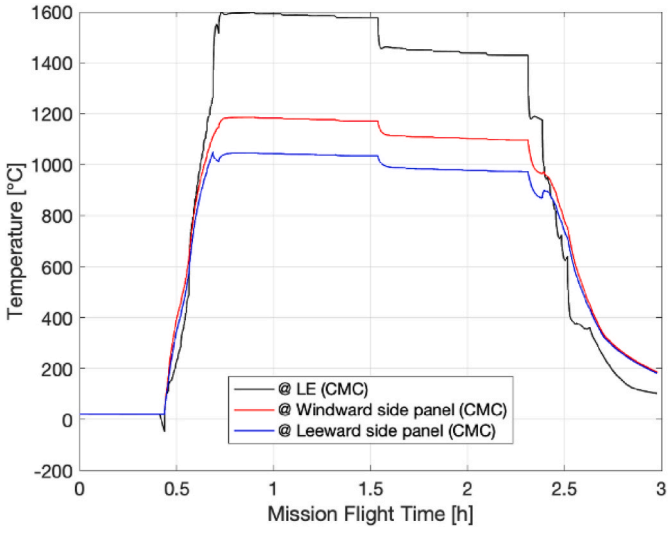

Fig. 18. (a) Maximum temperature evolution at CMC crotch and at CMC leeward side and windward side panel.

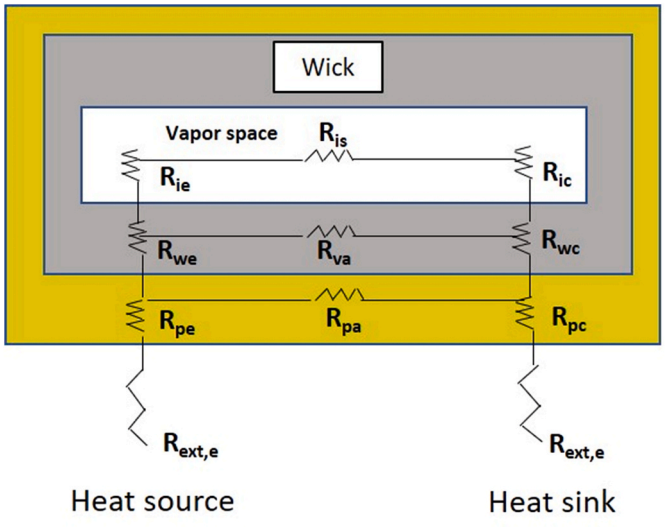

Fig. 19. Heat pipe lumped parametric model.

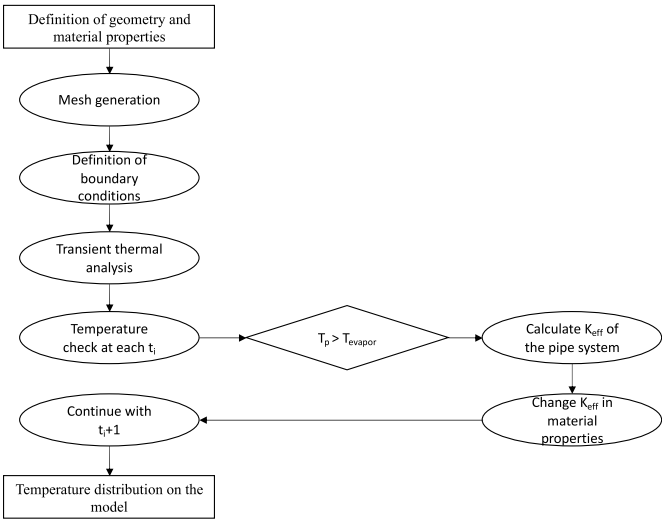

Fig. 20. Flow chart- simulation process.

maximum temperature at the interface between the crotch and the pipe structure. The temperature reaches a value of 1732 °C when the analysis is carried out without considering the pipe heat transfer cooling effect, instead 1421 °C is reached when pipe activation is considered.

Additionally, Fig. 24 shows the effective subtractive heat flux (in red) as evaluated in APDL. The average effective subtractive heat flux is about 0.72 MW/m^2 and it includes both the conductive and convective heat fluxes subtracted by the heat pipe. The conductive heat flux (in black) considers only the conduction contribution guaranteed by the presence of the heat pipe itself. Complementary, in blue, the convective subtractive heat flux due to pipe activation is of about 0.4 MW/m^2.

It is important to notice that the value of the effective subtractive heat flux derived by Pipe activation (0.72 MW/m^2) is in line with the most conservative value (0.7 MW/m^2) hypothesized during the thermal design step (the so-called run 1 in Fig. 16) (Fig. 25). (see Fig. 26).

5. Conclusions and future work

This paper presented the methodology and the preliminary results

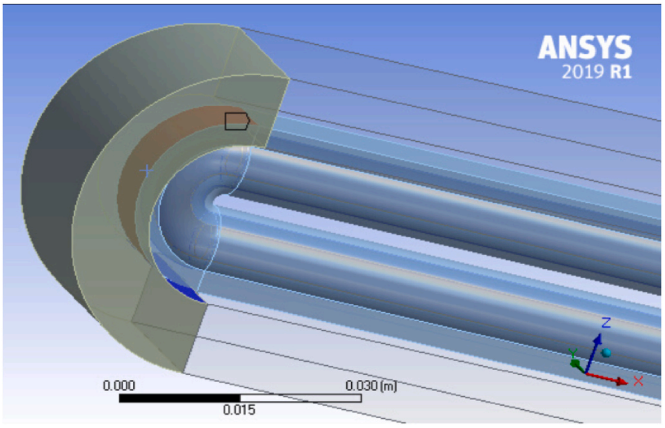

Fig. 23. Heat Flux control Point on the interface Crotch-Heat pipe.

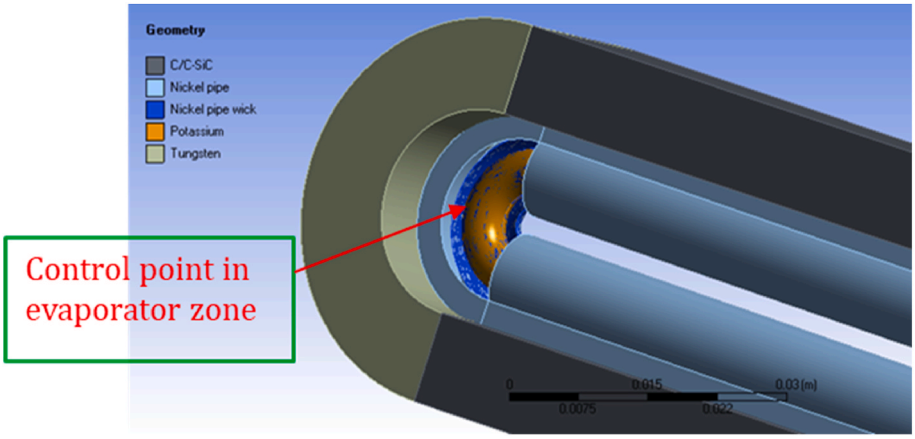

Fig. 21. Temperature control point in Evaporator zone.

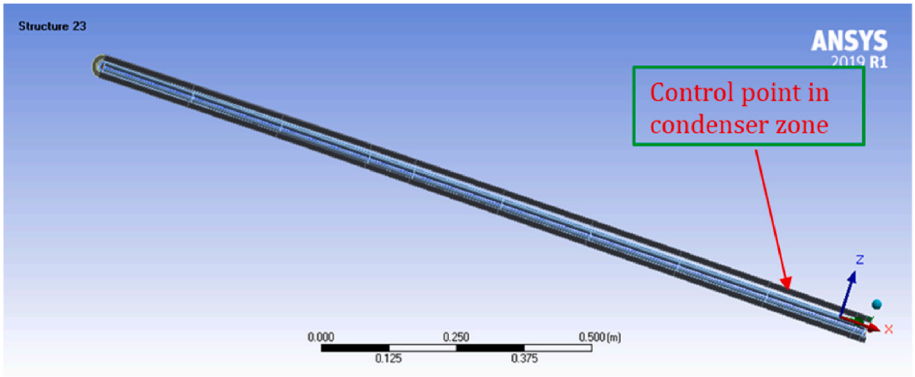

Fig. 22. Temperature control point in Condenser zone.

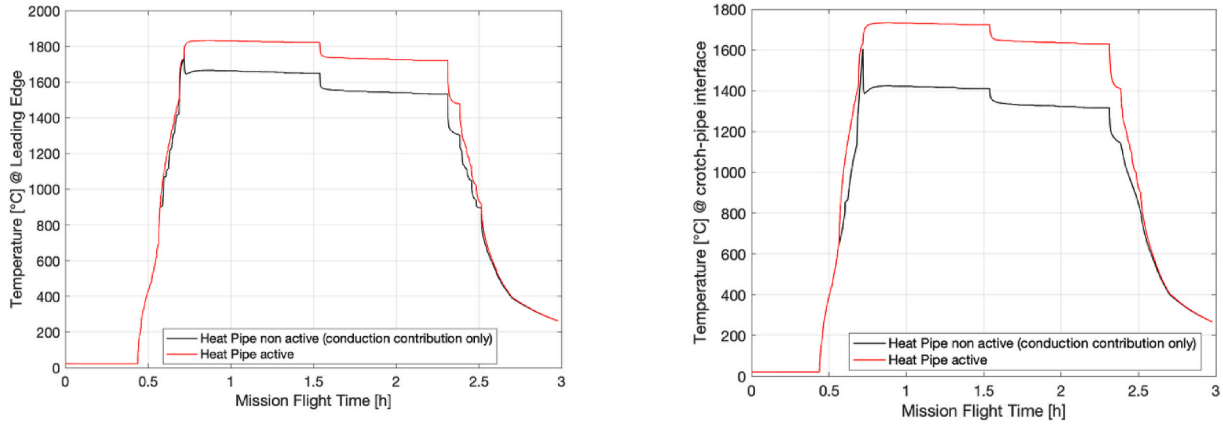

Fig. 24. (a) Maximum temperature evolution at CMC Leading edge w.r.t different thermal analysis; (b) Maximum temperature evolution at Interface Crotch/Pipe w.r.t different thermal analysis.

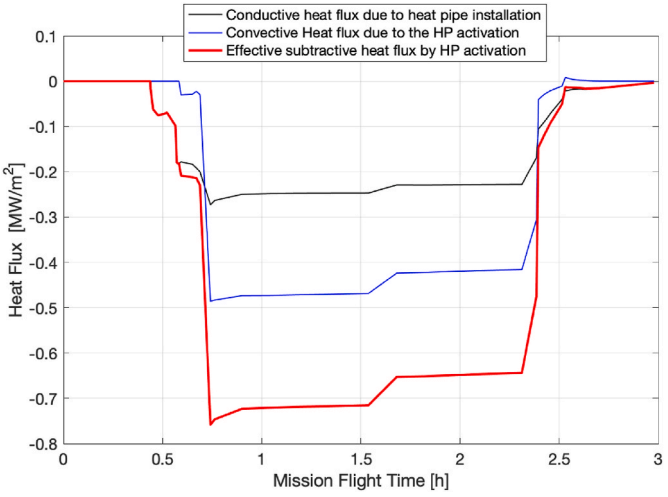

Fig. 25. Average Heat Flux evolution at crotch-Pipe interface w.r.t different thermal analysis.

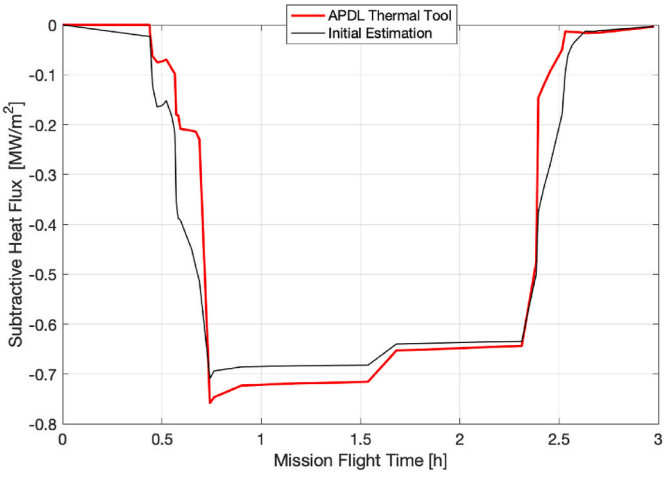

Fig. 26. Comparison of Subtractive Heat Flux estimation via APDL with reference to the initial guess.

achieved in the framework of the H2020 STRATOFLY Project in the design of the Thermal Protection System (TPS) of the MR3 vehicle. The results of the aero-thermal assessment performed throughout the trajectory with engineering formulations, as well as with dedicated CFD analysis, clearly indicate the air-intake leading edges as the most critical area, thus local TPS alternatives have been explored. Different alternative solutions have been thoroughly explored, including five liquid metals as fluids (Mercury, Caesium, Potassium, Sodium and Lithium) and relative wick and case materials (Steel, Titanium, Nickel, Inconel® and Tungsten) and three leading-edges materials (CMC, Tungsten with low emissivity painting and Tungsten with high emissivity painting). The analysis of the heat transfer limits (the capillary, entrainment, viscosity, chocking and boiling limits) carried out for all five fluids and relative compatible materials, together with a more accurate FEM analysis, have suggested the adoption of a Nickel–Potassium liquid metal heat pipe completely integrated in a platelet air-intake leading edge made of CMC material. The effectiveness of the adopted solution throughout all mission phases has been verified with a detailed numerical model, built upon an electrical analogy.

The results disclosed in this paper are highly interesting both from the theoretical and from the practical standpoints and they include relevant novelty aspects, as briefly summarized hereafter:

- The methodology disclosed in the paper has proved to perfectly fit the most up-to-date conceptual design approaches. Even if heat-pipe technologies and applications to high-speed transportation have already been thoroughly examined and reported in literature [32,33], none of the already available paperwork has disclosed an integrated conceptual design methodology able to anticipate the effect of heat pipes onto the vehicle performance. The application of such methodology to the STRATOFLY MR3 case study has revealed its crucial role to manage the increasing level of integration of future hypersonic systems as well as to deal with the worldwide incentive to dramatically shorten the design and development phases with a limited amount of time and budget resources.
- The implementation of a requirements' driven approach for the identification of feasibility areas in the design space and the subsequent synthetic visualization have shown to be very attractive for future applications. On one side, the preliminary heat pipe design and sizing disclosed in the paper is driven by the elicitation and analysis of design, interface and operational requirements. The application of the requirements driven approach to the STRATOFLY MR3 case study has demonstrated to be a powerful tool to support the trade-offs in terms of working fluid, materials, pipe arrangements, with first order quantitative estimations. On the other hand, the synthetic visualization of the design space which reports the maximum heat flux rejection capability as a function of the main design parameters, such as for example the wick radius, has proved to be a straightforward way to communicate the results achieved so far.

oThe possibility to anticipate the off-design behaviour, by analysing the heat pipe throughout an aircraft mission, has been deemed to be crucial especially in case of liquid metal heat pipes, where the duration of start-up phase cannot be neglected and substantial variations in pipe effectiveness can occur.
oThe verification of the effectiveness of the adopted solution throughout all mission phases, assessed with a detailed numerical model has proved to be a flexible tool with a broad spectrum of applications in the aerothermodynamic field.

Ultimately, it is worth notice that the multi-fidelity methodology disclosed and applied in this paper can be used to verify, since the conceptual design stage, the advantage of liquid metal heap pipe arrays for a wide range of hypersonic transportation systems, such as reusable access to space and re-entry systems and even for space transportation systems [38]. Further validation of these results with real world data, coming either from new experiments or from newly published literature can be part of future works on the topic.

Declaration of competing interest

The authors declare that they have no known competing financial interests or personal relationships that could have appeared to influence the work reported in this paper.

Acknowledgement

This research was funded by European Union's Horizon 2020 research and innovation programme under grant agreement No 769246 - Stratospheric Flying Opportunities for High-Speed Propulsion Concepts (STRATOFLY) Project.

References

[1] J. Steelant, R. Varvill, S. Defoort, K. Hannemann, M. Marini, Achievements obtained for sustained hypersonic flight within the LAPCAT-II project, Glasgow, Scotland, in: AIAA-2015-3677, 20th AIAA International Space Planes and Hypersonic Systems and Technologies Conference, 2015, 6-9 July.
[2] J. Steelant, ATLLAS: aero-thermal loaded material investigations for high-speed vehicles, in: 15th AIAA International Space Planes and Hypersonic Systems and Technologies Conference, 2008, p. 2582.
[3] J. Steelant. et al., Conceptual Design of the High-Speed Propelled Experimental Flight Test Vehicle HEXAFLY, 20th AIAA International Space Planes and Hypersonic Systems and Technologies Conference, Glasgow, Scotland, AIAA 2015-3539.
[4] S. Di Benedetto, et al., Multidisciplinary Design and Flight Test of the HEXAFLY-INT Experimental Flight Vehicle Hexafly-Int, in: HiSST: International Conference on High-Speed Vehicle Science Technology, 2018. Moscow, Russia.
[5] J.Y. Andro, R. Scigliano, A. Kallembach, J. Steelant, Thermal Management of the Hexafly-Int Hypersonic Glider, in: HiSST: International Conference on High-Speed Vehicle Science Technology, 2018. Moscow, Russia, November.
[6] R. Scigliano, S. Di Benedetto, M. Marini, V. Villace, J. Steelant, Hexafly-int hypersonic vehicle thermal protection system design, in: 71st International Astronautical Congress (IAC) – The CyberSpace Edition, October 2020, pp. 12–14. IAC-20-56572.
[7] Roberto Scigliano, Giuseppe Pezzella, Sara Di Benedetto, Marco Marini, Johan Steelant, HEXAFLY-INT Experimental Flight Test Vehicle (EFTV) Aero-Thermal Design, Tampa, FL, USA, in: ASME International Mechanical Engineering Congress & Exposition (IMECE), IMECE2017-70392, 2017. November 3-9.
[8] N. Viola, R. Fusaro, B. Saracoglu, C. Schram, V. Grewe, J. Martinez, C. Fureby, Main Challenges and Goals of the H2020 STRATOFLY Project, Aerotecnica Missili & Spazio, 2021, pp. 1–16.
[9] Viola, N., Fusaro, R., Gori, O., Marini, M., Roncioni, P., Saccone, G., Saracoglu, B., Ispir, A.C., Fureby, C., Nilsson, T., Ibron, C., Zettervall, N., Bates, K.N., Vincent, A., Martinez-Schram, J., Grewe, V., Pletzer, J., Hauglustaine, D., Linke, F., Bodmer, D. Stratofly MR3 – how to reduce the environmental impact of high-speed transportation, (2021) AIAA Scitech 2021 Forum, pp. 1-21.
[10] R. Fusaro, D. Ferretto, N. Viola, V.F. Villace, J. Steelant, A methodology for preliminary sizing of a Thermal and Energy Management System for a hypersonic vehicle, Aeronaut. J. 123 (1268) (2019) 1508–1544, https://doi.org/10.1017/aer.2019.109.
[11] C.C. Silverstein, A Feasibility Study of Heat-Pipe-Cooled Leading Edges for Hypersonic Cruise Aircraft, 1971. NASA/CR-1857.
[12] C.J. Camarda, Analysis and Radiant Heating Tests of a Heat-Pipe-Cooled Leading Edge NASA/TN D.-8468, 1977.
[13] C.J. Camarda, Application of Formal Optimization Techniques in Thermal/Structural Design of a Heat-Pipe-Cooled Panel for a Hypersonic Vehicle, 1987. NASA/TM-81931.
[14] D.E. Glass, M.A. Merrigan, J.T. Sena, Fabrication and Testing of a Leading-Edge-Shaped Heat Pipe, NASA/CR-208720, 1998.
[15] G.A. Steeves, M.Y. He, S.D. Kasen, Feasibility of metallic structural heat pipes as sharp leading edges for hypersonic vehicles, ASME J. Appl. Mech. 76 (2009), 031014-1e031014-12.
[16] G. Xiao, Y. Du, Y. Gui, L. Liu, X. Yang, D. Wei, Heat transfer characteristics and limitations analysis of heat-pipecooled thermal protection structure, Appl. Therm. Eng. 70 (2014) 655–664.
[17] D.E. Glass, Ceramic Matrix Composite (CMC) Thermal Protection Systems (TPS) and Hot Structures for Hypersonic Vehicles, AIAA-2008-268.
[18] A. Faghri, Heat Pipe Science and Technology, CRC Press, New York, 1995.
[19] L. Hongpeng, L. Weiqiang, Thermal–structural analysis of the platelet heat-pipe-cooled leading edge of hypersonic vehicle, Acta Astronaut. 127 (2016) 13–19.
[20] Fusaro, R., Ferretto, D., Viola, N. Model-Based Object-Oriented systems engineering methodology for the conceptual design of a hypersonic transportation system (2016) ISSE 2016 - 2016 International Symposium on Systems Engineering - Proceedings Papers, art. no. 7753175, DOI: 10.1109/SysEng.2016.7753175.
[21] R. Fusaro, N. Viola, High level requirements impact on configuration trade-off analyses in a multidisciplinary integrated conceptual design methodology, in: 2018 Aviation Technology, Integration, and Operations Conference, Art. No. AIAA 2018-4134, 2018, p. 17, https://doi.org/10.2514/6.2018-4134.
[22] R. Fusaro, N. Viola, D. Ferretto, V. Vercella, V. Fernandez Villace, J. Steelant, Life cycle cost estimation for high-speed transportation systems, CEAS Space J. 12 (2) (2020) 213–233, https://doi.org/10.1007/s12567-019-00291-7.
[23] T. Langener, S. Erb, J. Steelant, H. Flight, Trajectory simulation and optimization of the LAPCAT MR2 hypersonic cruiser concept, ICAS 2014 (2014) 428.
[24] N. Viola, P. Roncioni, O. Gori, R. Fusaro, Aerodynamic characterization of hypersonic transportation systems and its impact on mission analysis, Energies 14 (2021) 3580, https://doi.org/10.3390/en14123580.
[25] E.V. Zoby, J.N. Moss, K. Sutton, Approximate convective-heating equations for hypersonic flows, J. Spacecraft Rockets 18 (1) (1981) 64–70.
[26] N. Viola, R. Fusaro, O. Gori, M. Marini, P. Roncioni, G. Saccone, B. Saracoglu, A. C. Ispir, C. Fureby, T. Nilson, et al., STRATOFLY MR3–how to reduce the environmental impact of high-speed transportation, in: Proceedings of the A I A A Scitech 2021 Forum, 2021, p. 1877, https://doi.org/10.2514/6.2021-1877, 1 1 January.
[27] D. Ferretto, R. Fusaro, N. Viola, Innovative Multiple Matching Charts approach to support the conceptual design of hypersonic vehicles, Proc. Inst. Mech. Eng. Part G J. Aerosp. Eng. 234 (2020) 1893–1912, https://doi.org/10.1177/0954410020920037.
[28] Ferretto, D.; Fusaro, R.; Viola, N. A conceptual design tool to support high-speed vehicle design. In Proceedings of the AIAA AVIATION 2020 FORUM, 15–19 June 2020 Virtual Event; p. 2647, doi:10.2514/6.2020-2647.
[29] R. Scigliano, V. De Simone, M. Marini, P. Roncioni, R. Fusaro, N. Viola, Preliminary finite element thermal analysis of STRATOFLY hypersonic vehicle, 23rd AIAA International Space Planes and Hypersonic Systems and Technologies Conference - AIAA HYPERSONICS 2020, March 10-12, 2020, (Montreal, Quebec, Canada).
[30] R. Scigliano, M. Marini, P. Roncioni, R. Fusaro, N. Viola, STRATOFLY high-speed propelled vehicle preliminary aero-thermal design, international conference on flight vehicles, Monopoli (Italy), in: Aerothermodynamics and Re-entry Missions and Engineering FAR 2019, 2019, 30th September - 3rd October.
[31] R. Scigliano, M. Marini, R. Fusaro, N. Viola, Preliminary aero-thermal assessment of the high-speed propelled vehicle STRATOFLY, in: 32nd ISTS (International Symposium on Space Technology and Science) & 9th NSAT (Nano-Satellite Symposium), June 2019. Fukui (Japan).
[32] B. Zahuri, Heat Pipe Design and Technology – A Practical Approach, CRC Press, New York, 2011.
[33] P.J. Brennan, E.J. Kroliczek, Heat Pipe Design Handbook – Volume I, B&K Engineerin Inc., Towson (MD), 1979.
[34] A. Abo El-Nasr, S.M. El-Haggar, Effective thermal conductivity of heat pipes, Heat Mass Tran. 32 (1996) 97–101 (Springer-Verlag), 1996.
[35] G.P. Peterson, An Introduction to Heat Pipes: Modeling, Testing, and Applications, Wiley, 1994, 22 September.
[36] F. Iorizzo, Coupling of Lumped and Distributed Parameter Models for Numerical Simulation of A Sintered Heat Pipe, POLIMI, Milano, 2011.
[37] H.H. Coe, Summary of Thermophysical Properties of Potassium, National Aeronautics and Space Administration, 1965.
[38] M. Mammarella, C.A. Paissoni, N. Viola, A. Denaro, E. Gargioli, F. Massobrio, The lunar space tug: a sustainable bridge between low earth orbits and the cislunar habitat, Acta Astronaut. 138 (2017) 102–117, https://doi.org/10.1016/j.actaastro.2017.05.034.
[39] C. Camarda, D.E. Glass, Thermostructural Applications of Heat Pipes for Cooling Leading Edges of High-Speed Aerospace Vehicles, NASA Technical Report, Hampton, VA, USA, 1992.